Master's thesis
Theoretical physics

Weak Gravitational Lensing and Cosmology

Clint M. Gibson
October 2017

Advisor: Hannu Kurki-Suonio
Censors: Hannu Kurki-Suonio
Kari Enqvist

UNIVERSITY OF HELSINKI
DEPARTMENT OF PHYSICS

PL 64 (Gustaf Hällströmin katu 2)
00014 University of Helsinki

HELSINGIN YLIOPISTO — HELSINGFORS UNIVERSITET — UNIVERSITY OF HELSINKI

Tiedekunta/Osasto — Fakultet/Sektion — Faculty	Laitos — Institution — Department
Faculty of Science	Department of Physics

Tekijä — Författare — Author
Clint M. Gibson

Työn nimi — Arbetets titel — Title

Weak Gravitational Lensing and Cosmology

Oppiaine — Läroämne — Subject
Theoretical physics

Työn laji — Arbetets art — Level	Aika — Datum — Month and year	Sivumäärä — Sidoantal — Number of pages
Master's thesis	October 2017	87

Tiivistelmä — Referat — Abstract

Albert Einstein's General Theory of Relativity radically transformed our understanding of gravitation. Along with this transformative view came several powerful predictions. One of these predictions, the deflection of light in a gravitational field, has proven in recent decades to be crucial to the study of cosmology. In this work we present the foundational theory of gravitational lensing, with a particular focus on the weak regime of lensing. Weak gravitational lensing produced by the large scale structure, called cosmic shear, induces percent level distortions in the images of distant galaxies. Gravitational lensing is of particular interest, since the image distortions are due to all of the matter in the large scale structure, including dark matter. We present the definitions of shear and convergence which are used to quantify the source galaxy image distortions, and discuss some techniques shown in literature which are used for measuring these quantities. This includes presenting the necessary derivations which connect these quantities to two particular classes of results: mass map reconstructions and cosmological parameter constraints. We present some results obtained in recent years: mass map reconstructions obtained using the Canada-France-Hawaii-Telescope Lensing Survey (CFHTLenS) and the Cosmological Evolution Survey (COSMOS), and constraints on the parameters Ω_m and σ_8 (the total matter density parameter and the power spectrum normalization) obtained using CFHTLenS, COSMOS, the Kilo Degree Survey (KiDS), and the Dark Energy Survey (DES). This includes some discussion of apparent tensions with results obtained from Planck (using observations of the cosmic microwave backgroundâĂŤa completely different cosmological probe) and of some inconsistencies within the more recent survey results.

Avainsanat — Nyckelord — Keywords
cosmology, gravitational lensing, dark matter, large-scale structure, cosmic shear

Säilytyspaikka — Förvaringsställe — Where deposited
Kumpula Campus Library

Muita tietoja — Övriga uppgifter — Additional information

Contents

Chapter 1

Introduction

When Albert Einstein proposed his General Theory of Relativity (hereafter, GR) in 1915, he put forth a radically new picture of gravity (Einstein 1916). His theory was first tested a few years later, following World War I, when Arthur Eddington and his team measured the deflection of starlight grazing the surface of the Sun, and it was shown to have the value predicted by Einstein's theory (Dyson, Eddington, and Davidson 1920). In the decades since, this and other predictions of the theory have been tested and confirmed many times over, and we now understand gravitational attraction to be the result of distortions in spacetime due to the presence of mass.

Now, nearly a century later, in addition to forming the foundation of our modern understanding of gravity, GR is proving to be a valuable tool in the study of cosmology. When we look out into the universe, and especially when we look at very distant galaxies, we do not see objects as they truly are. That is, they do not appear to us as they would without the spacetime distortions of GR because, as shown by that first test in 1919, the light from these distant galaxies will also be

affected by the distortions. A bundle of light rays leaving a distant galaxy will be reshaped many times by the distribution of matter which occupies the intervening space between the galaxy and us observers here on Earth. It is by observing and quantifying these image distortions that we probe the nature of the structures which caused them.

The first detection of this type of distortion, which we call *gravitational lensing*, was actually made in 1979 by Walsh, Carswell, and Weymann (1979) who observed a doubly-imaged "blue stellar object" (quasar) being lensed by a galaxy. In the years since, the invention of better and more precise telescopes and imaging equipment have enabled us to detect even smaller lensing distortions. In the treatise that follows we will be investigating this latter case of *weak gravitational lensing*. In Chapter 2 we will review the principles of general gravitational lensing, and show derivations of equations and definitions of quantites relevant to the analysis of lensing obervations. In Chapter 3 we will continue with the discussion of lensing, but narrow the focus to the case of weak lensing due to the inhomogeneous matter distribution (i.e. *cosmological lensing* or *cosmic shear*). In particular, we will present some of the primary statistical measures which are used to interpret data from cosmic shear surveys. In Chapter 4 we then present some results from the Canada-France-Hawaii Telescope Lensing Survey (CFHTLenS) (Heymans et al. 2012; Erben et al. 2013) and the Cosmic Evolution Survey (COSMOS) (Scoville et al. 2007), and more recently from the Kilo Degree Survey (KiDS) (de Jong et al. 2013) and the Dark Energy Survey (DES) (The Dark Energy Survey Collaboration 2005). In Chapter 5 we look ahead at some future surveys which we hope will provide us with still more accurate data with which to perform lensing analyses and probe the cosmos. Finally, in Chapter 6 we will present conclusions and summarize the main points of this work.

Chapter 2

Principles of Gravitational Lensing

In this chapter we will review those principles of gravitational lensing which are relevant to the results presented later in Chapter 4. The bulk of the discussion is similar to that given by Schneider, Wambganss, and Kochanek (2006) (SWK, hereafter), but with adapted notation.

2.1 General Relativity and Light Deflection

Fundamental to the understanding of gravitational lensing is the phenomenon of light deflection due to the distortion of space-time. According to the general theory of relativity, the presence of a matter-energy density will distort the space around it such that it is no longer Minkowskian. If we assume that the mass is electrically neutral, spherically symmetric, and non-rotating then it can be shown, starting from the Schwarzschild metric

$$ds^2 = -\left(1 - \frac{2GM}{r}\right) c^2 dt^2 + \frac{dr^2}{1 - \frac{2GM}{r}} + r^2 d\theta^2 + r^2 \sin^2\theta d\phi^2, \qquad (2.1)$$

that a single light ray as it passes the distorting mass will be deflected by the angle

$$\tilde{\alpha}(r) = \frac{4GM}{rc^2} \tag{2.2}$$

for

$$r \gg \frac{4GM}{c^2}, \tag{2.3}$$

where G is Newton's gravitational constant, M is the distorting mass, c is the speed of light, and r is the impact parameter (distance of closest approach of the light ray to the distorting mass). Now, in reality the path followed by a light ray from the source to the observer is curved. However, when the separation distances between the source, distorting mass (or *lens*), and observer are large (compared to r), the *thin lens* approximation can be made, where the path is assumed to be composed of two straight line segments (see Figure 2.1).

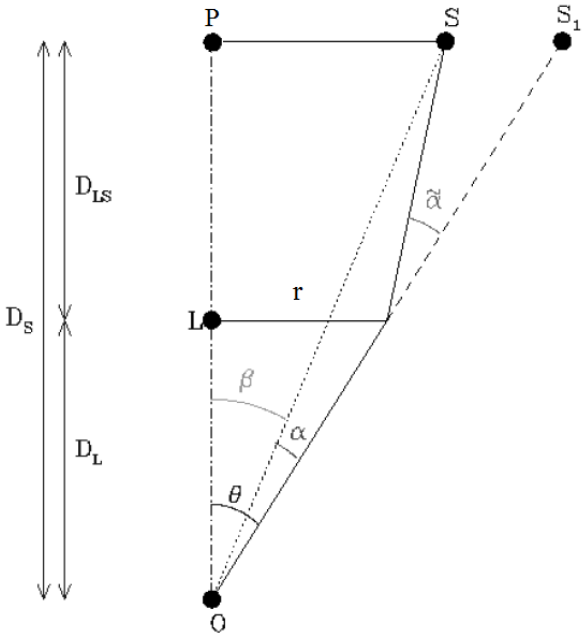

Figure 2.1: (Adapted from Figure 1 of Heavens (2011).) The lens geometry, showing the location of the source S and image S_1 with respect to the distorting mass at L and the observer O.

2.2 Lensing Due to a Point Mass

In Figure 2.1 one can clearly see that the distances $\overline{PS}_1, \overline{PS}$, and $\overline{SS}_1$ are be related by $\overline{PS}_1 = \overline{PS} + \overline{SS}_1$. These distances can then be related to the angles $\tilde{\alpha}, \beta$, and θ and we can write

$$D_S\theta = D_S\beta + D_{LS}\tilde{\alpha}, \tag{2.4}$$

where the small angle approximation has been used. If we further define a new angle α (the *scaled deflection angle*) between the source and the image as

$$\alpha = \frac{D_{LS}}{D_S}\tilde{\alpha} \tag{2.5}$$

then we can rewrite (2.4) as

$$\beta = \theta - \alpha \tag{2.6}$$

to obtain the so-called *lens equation*. The lens equation thus relates the source position (β) to the image position (θ) and the scaled deflection angle. In the case of a point-mass deflector, the bend angle defined in (2.2) holds, since a point-mass is a special case of the more general spherically symmetric mass, and the angle α can be written as

$$\alpha(\theta) = \frac{4GM}{c^2\theta}\frac{D_{LS}}{D_L D_S} \tag{2.7}$$

where the small angle approximation has again been used to write $r = D_L\theta$. This result is valid as long as the light ray remains outside of the distorting mass. If we further define the *Einstein angle* (Heavens 2011)

$$\theta_E = \sqrt{\frac{4GM}{c^2}\frac{D_{LS}}{D_L D_S}}, \tag{2.8}$$

then the lens equation can be rewritten as a quadratic equation in θ,

$$\theta^2 - \beta\theta - \theta_E^2 = 0, \tag{2.9}$$

which can be solved analytically for θ to obtain

$$\theta = \frac{\beta}{2} \pm \sqrt{\frac{\beta^2}{4} + \theta_E^2}. \tag{2.10}$$

Now, referring back to Figure 2.1 we see that θ gives the position of the *image*, which is what the observer will actually see. Based on the result in (2.10), then, this means that the observer will see the same object at two different positions on the sky! A particularly clean (and dramatic) example of this is shown in Figure 2.2.

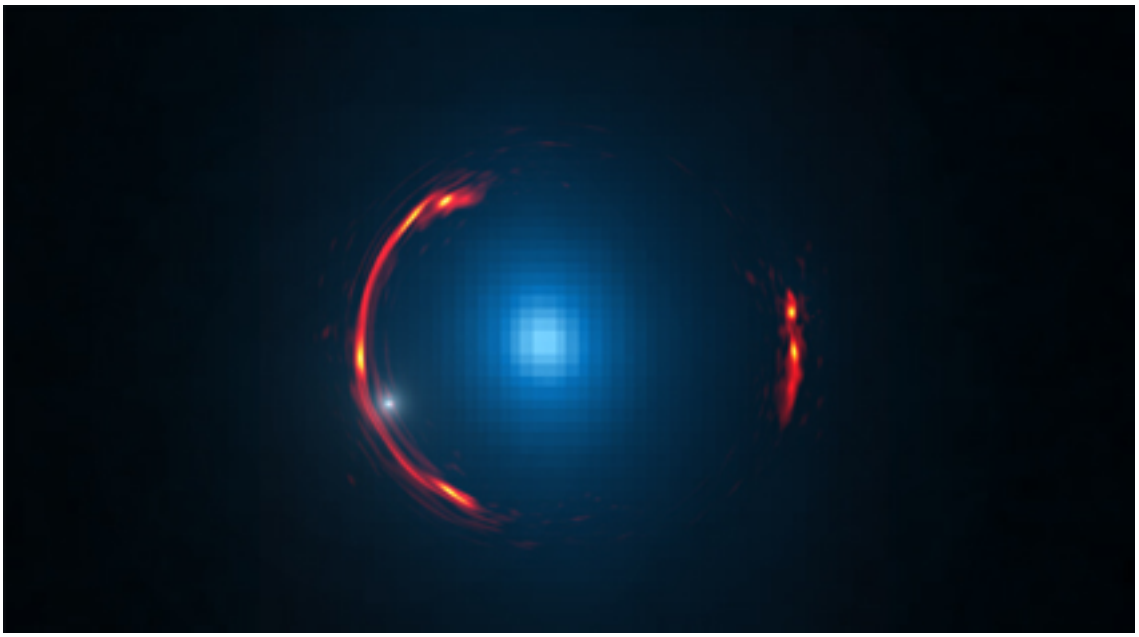

Figure 2.2: Gravitational lens SDP.81. Composite image depicting a distant galaxy, appearing as red arcs, lensed by a nearby galaxy, appearing as a blue dot.

2.3 Gravitational Thin Lens

Now, realistically a light ray travelling through the universe will not be deflected by a single point mass, but rather is subjected to deflection due to a number of masses.

In this section we will extend the discussion of bend angle from the previous section to that of a thin mass distribution (that is, the variations in D_L are small compared to D_L and D_{LS}). We will additionally be assuming that the deflection angles are small, such that we are considering the case of the *gravitational thin lens*. Under this so-called *Born approximation*, successive deflections are additive.

2.3.1 Deflection Angle Due to a Thin Lens

We saw in the previous section that the deflection angle of a light ray as it passes by a deflecting mass is determined by the mass of the deflector and the distance of closest approach. The result given by (2.2) was an angle lying in the plane of the observer, lens, and source in Figure 2.1. When we introduce additional deflecting masses (say, at the same radial distance from the observer), the deflection angle is determined by summing the contributions from all of the masses. Futhermore, the subtended angle is now described by a vector quantity.

Let us define the coordinate $\boldsymbol{r} = (r_1, r_2)$ which is a vector describing the point of incidence of the light ray on the *lens plane* (see Figure 2.3). (Note that here and throughout this text, vectors are indicated with **bold** typeface.) Now, for a collection of N masses at positions $\boldsymbol{R'} = (\boldsymbol{r}, r'_3) = (r'_1, r'_2, r'_3)$, the total vector deflection angle will be (SWK, p.19)

$$\tilde{\boldsymbol{\alpha}}(\boldsymbol{r}) = \frac{4G}{c^2} \sum_N m(\boldsymbol{R'}) \frac{\boldsymbol{r} - \boldsymbol{r'}}{|\boldsymbol{r} - \boldsymbol{r'}|^2} \tag{2.11}$$

so that $\boldsymbol{r} - \boldsymbol{r'}$ is the vector impact parameter of the light ray for each mass at $\boldsymbol{r'}$.

If we then consider the deflection due to a mass *distribution*, we sum over the mass elements $dm = \rho(\boldsymbol{R'})dV$, and (2.11) becomes the integral formula

$$\tilde{\boldsymbol{\alpha}}(\boldsymbol{r}) = \frac{4G}{c^2} \int d^2r' \int \rho(r'_1, r'_2, r'_3) \frac{\boldsymbol{r} - \boldsymbol{r'}}{|\boldsymbol{r} - \boldsymbol{r'}|^2} dr'_3 \tag{2.12}$$

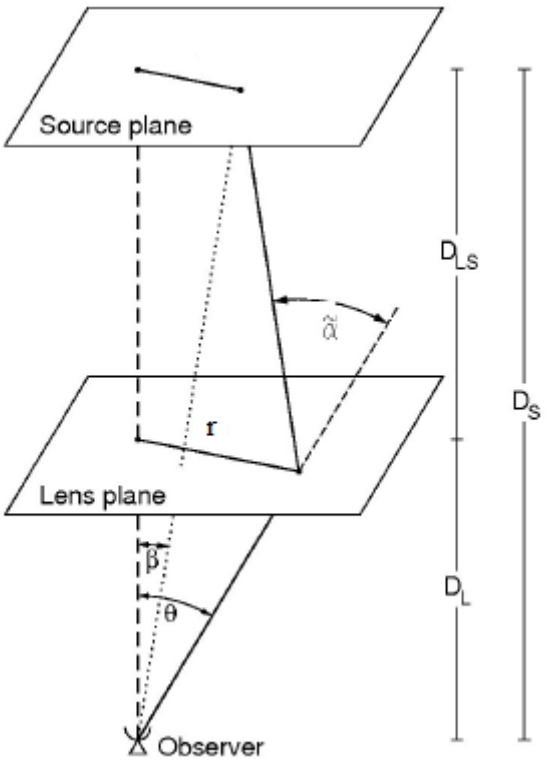

Figure 2.3: Geometry of a thin (two dimensional) lens.

where the integration has been split into the integrals on the lens plane (d^2r') and off of the lens plane along the propogation of the light ray (dr'_3). But, remember that here we are supposed to be treating the case of a 2D thin lens, so that the variation in r'_3 is much less than D_S. Notice that the factor in the above equation containing the vector impact parameter does not depend on r'_3. We can thus define the *surface mass density* as (SWK, p.19)

$$\Sigma(r_1, r_2) \equiv \int \rho(r_1, r_2, r_3) dr_3. \tag{2.13}$$

So the totality of the deflecting mass distribution has been projected onto a 2D plane, the *lens plane*, and thus the lens is treated as being a two dimensional thin lens. The deflection angle (which is a two dimensional vector quantity, and

orthogonal to the line of sight) is then (SWK, p.19)

$$\tilde{\boldsymbol{\alpha}}(\boldsymbol{r}) = \frac{4G}{c^2}\int \Sigma(\boldsymbol{r'})\frac{\boldsymbol{r}-\boldsymbol{r'}}{|\boldsymbol{r}-\boldsymbol{r'}|^2}d^2r'. \tag{2.14}$$

2.3.2 The Lens Equation for a Thin Lens

In a previous section we defined the *lens equation* (2.6), and showed how it could be solved analytically for the simple case of a point mass deflector. We will now look again at the lens equation for the more general case of a thin deflector (as defined previously). We can first rewrite (2.14) using the definition in (2.5) to get

$$\boldsymbol{\alpha}(\boldsymbol{r}) = \frac{4G}{c^2}\frac{D_{LS}}{D_S}\int \Sigma(\boldsymbol{r'})\frac{\boldsymbol{r}-\boldsymbol{r'}}{|\boldsymbol{r}-\boldsymbol{r'}|^2}d^2r'. \tag{2.15}$$

Next, continuing with the small angle approximation, we can rewrite $\boldsymbol{r}$ in terms of $\boldsymbol{\theta}$ as $D_L\boldsymbol{\theta}$ (and likewise $\boldsymbol{r'} = D_L\boldsymbol{\theta'}$). We can then factor out and cancel common factors of D_L so that we are left with one factor of D_L in the numerator. This gives

$$\boldsymbol{\alpha}(\boldsymbol{\theta}) = \frac{4G}{c^2}\frac{D_{LS}D_L}{D_S}\int \Sigma(\boldsymbol{\theta'})\frac{\boldsymbol{\theta}-\boldsymbol{\theta'}}{|\boldsymbol{\theta}-\boldsymbol{\theta'}|^2}d^2\theta'. \tag{2.16}$$

If we now define the *critical surface mass density*, Σ_{crit}, as

$$\Sigma_{crit} = \frac{c^2}{4\pi G}\frac{D_S}{D_{LS}D_L} \tag{2.17}$$

and define the *convergence* as

$$\kappa(\boldsymbol{\theta}) \equiv \frac{\Sigma(\boldsymbol{\theta})}{\Sigma_{crit}}, \tag{2.18}$$

the bend angle can finally be written as (SWK, p.21)

$$\boldsymbol{\alpha}(\boldsymbol{\theta}) = \frac{1}{\pi}\int \kappa(\boldsymbol{\theta'})\frac{\boldsymbol{\theta}-\boldsymbol{\theta'}}{|\boldsymbol{\theta}-\boldsymbol{\theta'}|^2}d^2\theta'. \tag{2.19}$$

So, in the case of a thin lens, the lens equation (2.6) becomes a vector equation, $\boldsymbol{\beta} = \boldsymbol{\theta} - \boldsymbol{\alpha}(\boldsymbol{\theta})$. It should be noted that, while we were able to find an analytic

solution to the equation in the simple case of a point mass lens (that is, we found the image positions θ in terms of the given source location β), this is not generally possible.

It is important to remember that here and in the rest of this work, the angles $\boldsymbol{\alpha}, \boldsymbol{\beta}$ and $\boldsymbol{\theta}$ are actually two dimensional vectors (in either the lens or source plane). It may be unusual to think of angles as vectors; however, remember that the distances between the observer, lens, and source which we are dealing with are quite large compared to the size of these objects. Since we are thus concerned with small sections of the sky, we can think of these regions as planes rather than having to consider them as spherical surfaces.

2.4 Distortion and Magnification of Images

Thus far the discussion has been focussed on the behavior of a single light ray as it passes from the source to the observer, but a source such as a star or galaxy obviously is emitting more than a single light ray. In this section we will begin to consider what happens to the image of an extended source when its light is subjected to the lensing effects described above.

2.4.1 Differential Light Deflection

When we look at an extended object, the light from various parts of that object meet our eye (or telescope, camera, etc.) at different angles. If we consider just the outline of such an object then this is how we can judge its shape, in the absence of lensing, and also its size assuming we know how far away it is. An example with

a simple "stick"-like object is shown in Figure 2.4. For ease, we will just consider a point-mass deflector for illustration purposes. The observer can determine how long it is using the observed angle between the ray from the top (A) and from the bottom (B). Now, if a lensing mass is present in the intervening space then both light rays A and B will be deflected such that the observed angle between them is greater, thus stretching the image that reaches the observer.

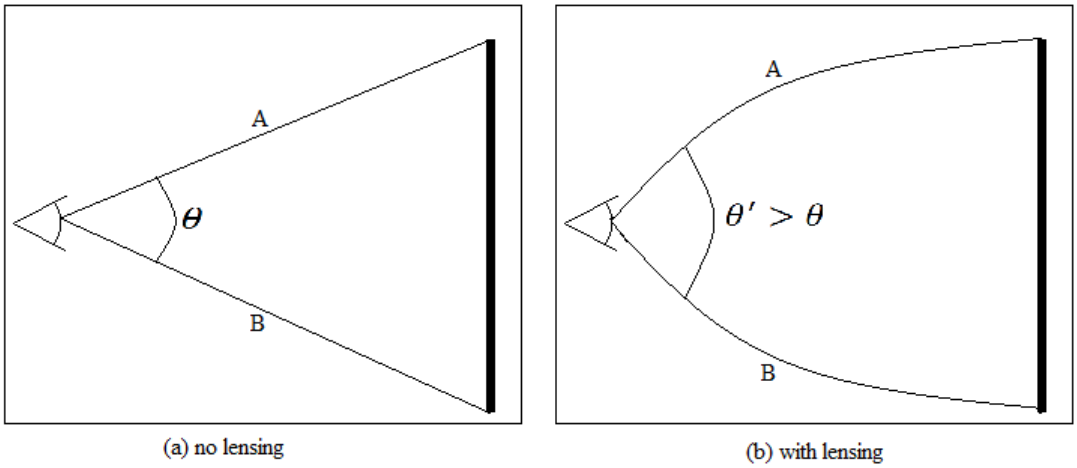

Figure 2.4: The image of a "stick"-like object being stretched due to a point mass lense.

We can also consider the case of two light rays, presumably coming from opposite edges of an extended source, which pass by a lensing mass at different distances. Since rays passing by at different distances are bent at different angles, according to (2.2), there will also be an effect on the observed distance between the source points in this direction. So, light rays from extended sources, passing near lensing masses with varying impact parameters, will undergo varying amounts of deflection. That is, *light bundles from sources will be deflected differentially.* Thus, the images received by the observer will be distorted.

2.4.2 The Amplification Matrix

Let us now quantify the distortion effect of images due to lensing. To begin we will need to define a new quantity, the *lensing potential* (SWK, p.22)

$$\psi(\boldsymbol{\theta}) = \frac{1}{\pi}\int \kappa(\boldsymbol{\theta'}) \ln|\boldsymbol{\theta} - \boldsymbol{\theta'}| d^2\theta'. \tag{2.20}$$

The identity (A.1) $\nabla \ln|\boldsymbol{q}| = \frac{\boldsymbol{q}}{|\boldsymbol{q}|^2}$ holds for any two dimensional vector $\boldsymbol{q}$ (see Appendix A for proof). Then taking the gradient of the lensing potential we get

$$\nabla\psi(\boldsymbol{\theta}) = \frac{1}{\pi}\int \kappa(\boldsymbol{\theta'}) \frac{\boldsymbol{\theta} - \boldsymbol{\theta'}}{|\boldsymbol{\theta} - \boldsymbol{\theta'}|^2} d^2\theta', \tag{2.21}$$

so

$$\boldsymbol{\alpha}(\boldsymbol{\theta}) = \nabla\psi(\boldsymbol{\theta}). \tag{2.22}$$

Furthermore let us take the Laplacian of both sides of (2.20). We can apply the identity (A.2) $\nabla^2 \ln|\boldsymbol{q}| = 2\pi\delta_D(\boldsymbol{q})$, thus forcing $\boldsymbol{\theta'} = \boldsymbol{\theta}$ upon taking the integral, so that we get

$$\nabla^2\psi(\boldsymbol{\theta}) = 2\kappa(\boldsymbol{\theta}). \tag{2.23}$$

The distortion of images can be described by the *amplification* matrix, whose elements are (SWK, p.23)

$$A_{ij}(\boldsymbol{\theta}) \equiv \frac{\partial\beta_i}{\partial\theta_j} = \delta_{ij} - \frac{\partial^2\psi(\boldsymbol{\theta})}{\partial\theta_i\partial\theta_j}, \tag{2.24}$$

where we have used the vector lens equation and the relation between ψ and $\boldsymbol{\alpha}$ found earlier. The delta function arises due to the orthogonality of the directions θ_i and θ_j. Also note that this is the Jacobian matrix, since we are transforming from coordinates on the source plane ($\boldsymbol{\beta}$) to ones on the lens plane ($\boldsymbol{\theta}$). If we look

just at the $i = 1, j = 1$ component we have

$$\begin{aligned} A_{11} &= 1 - \frac{\partial^2 \psi}{\partial \theta_1^2} \\ &= 1 - \frac{1}{2}\frac{\partial^2 \psi}{\partial \theta_1^2} - \frac{1}{2}\frac{\partial^2 \psi}{\partial \theta_1^2} - \frac{1}{2}\frac{\partial^2 \psi}{\partial \theta_2^2} + \frac{1}{2}\frac{\partial^2 \psi}{\partial \theta_2^2} \\ &= 1 - \frac{1}{2}\left(\frac{\partial^2 \psi}{\partial \theta_1^2} + \frac{\partial^2 \psi}{\partial \theta_2^2}\right) - \frac{1}{2}\left(\frac{\partial^2 \psi}{\partial \theta_1^2} - \frac{\partial^2 \psi}{\partial \theta_2^2}\right) \\ &= 1 - \kappa - \gamma_1 \end{aligned} \tag{2.25}$$

where we have used the relation between ψ and κ above. We have also defined the *shear* quantities $\gamma_1 = \frac{1}{2}\left(\frac{\partial^2 \psi}{\partial \theta_1^2} - \frac{\partial^2 \psi}{\partial \theta_2^2}\right)$ and $\gamma_2 = \frac{\partial^2 \psi}{\partial \theta_1 \partial \theta_2}$. It turns out that it is convenient to write the shear as a complex number, $\gamma = \gamma_1 + i\gamma_2$. The other components can be found in a similar fashion, and the amplification matrix can be written as

$$\boldsymbol{A}(\boldsymbol{\theta}) = \begin{bmatrix} 1 - \kappa & 0 \\ 0 & 1 - \kappa \end{bmatrix} + \begin{bmatrix} -\gamma_1 & -\gamma_2 \\ -\gamma_2 & \gamma_1 \end{bmatrix} \tag{2.26}$$

where the matrix has been split into the *convergence matrix* and the *shear matrix*. The convergence matrix contains information regarding the isotropic expansion or contraction of the image, while the shear matrix contains information regarding distortions in the overall shape of the image.

2.4.3 Magnification

Now that we have defined the *amplification matrix*, which quantifies the distortions induced on a source image due to lensing, we can go a step further and specifically quantify the *magnification* of the image. If we take the inverse of the amplification matrix, which is the Jacobian of the source- and lens-plane coordinates, then we get a mapping to the lens plane from the source plane. So by writing the amplification matrix as a single matrix, and using the fact that the determinant

of an inverse matrix is equal to the inverse of the determinant, we can calculate the magnification μ as (SWK, p.23)

$$\mu = \frac{1}{\det A} = \frac{1}{(1-\kappa)^2 - |\gamma|^2} \tag{2.27}$$

Assuming that no photons are emitted or absorbed during the journey from the source to the observer, then according to the Liouville Theorem the surface brightness of the source will be conserved (SWK, p.23). This means, then, that when an image is magnified due to lensing there will necessarily be a corresponding *amplification*. That is, it will make the background objects appear brighter, making faint objects easier to see. It can even mean that objects will become visible which would have otherwise been too faint even to detect.

2.5 Principles of Weak Lensing

We will now turn our attention to the more specific case of lensing called *weak gravitational lensing*. In the *strong* lensing regime we see the spectacular effects like the giant arcs in Figure 2.2, multiple images, and Einstein rings. In the weak lensing regime, however, the distortion effects are much less drastic. We will first peruse some general principles of weak lensing, expanding on the theoretical description given above.

2.5.1 Weak Lensing Geometry

Let us first recall the amplification matrix, (2.26). Next we define a quantity called the *reduced shear* $g = g_1 + ig_2$, the components of which are

$$g_i \equiv \frac{\gamma_i}{1-\kappa}. \tag{2.28}$$

If we then rewrite the amplification matrix as a single matrix, swap out the γ_i with $g_i\,(1-\kappa)$, and factor out the $1-\kappa$ from each element, we obtain (SWK, p.24)

$$\boldsymbol{A}(\boldsymbol{\theta}) = (1-\kappa)\begin{bmatrix} 1-g_1 & -g_2 \\ -g_2 & 1+g_1 \end{bmatrix}. \tag{2.29}$$

What we notice here is that the quantity containing information about the convergence is now represented as a multiplicative factor on the amplification matrix. So, shear measurements from weak lensing surveys, which are based only on the shapes of images, will actually be measuring the reduced shear g_i rather than the actual shear γ_i. However, we define the weak lensing regime as one in which $|\kappa| \ll 1$ so that $g_i \approx \gamma_i$ (Schneider 2005).

Let us discuss the components of the shear in a bit more detail. In the previous section it was stated that the shear quantifies the distortion of the image due to lensing. For the moment we will pretend that all of our sources are circles. Since the convergence corresponds to an isotropic expansion or contraction of the image, convergence in the absence of shear would result in simply a larger or smaller circle. Shear, on the other hand, will have a stretching effect causing our otherwise circular image to turn into an ellipse. The components of the shear actually describe the direction of this stretching. Naively one may suspect that g_1 and g_2 quantify the stretching in orthogonal directions, but in fact the component g_2 quantifies the stretching at *45 degrees* to g_1 (however, g_1 and g_2 are orthogonal in the *complex* plane). See Figure 2.5 for an illustration of the different effects of the individual shear components.

Now we write the reduced shear in the new form

$$g = |g|\mathrm{e}^{2i\phi}, \tag{2.30}$$

where we have introduced the new angle ϕ. Note that this angle is not a vector like $\boldsymbol{\theta}, \boldsymbol{\beta}$, and $\boldsymbol{\alpha}$, as those angles were coordinates on the lens and source planes.

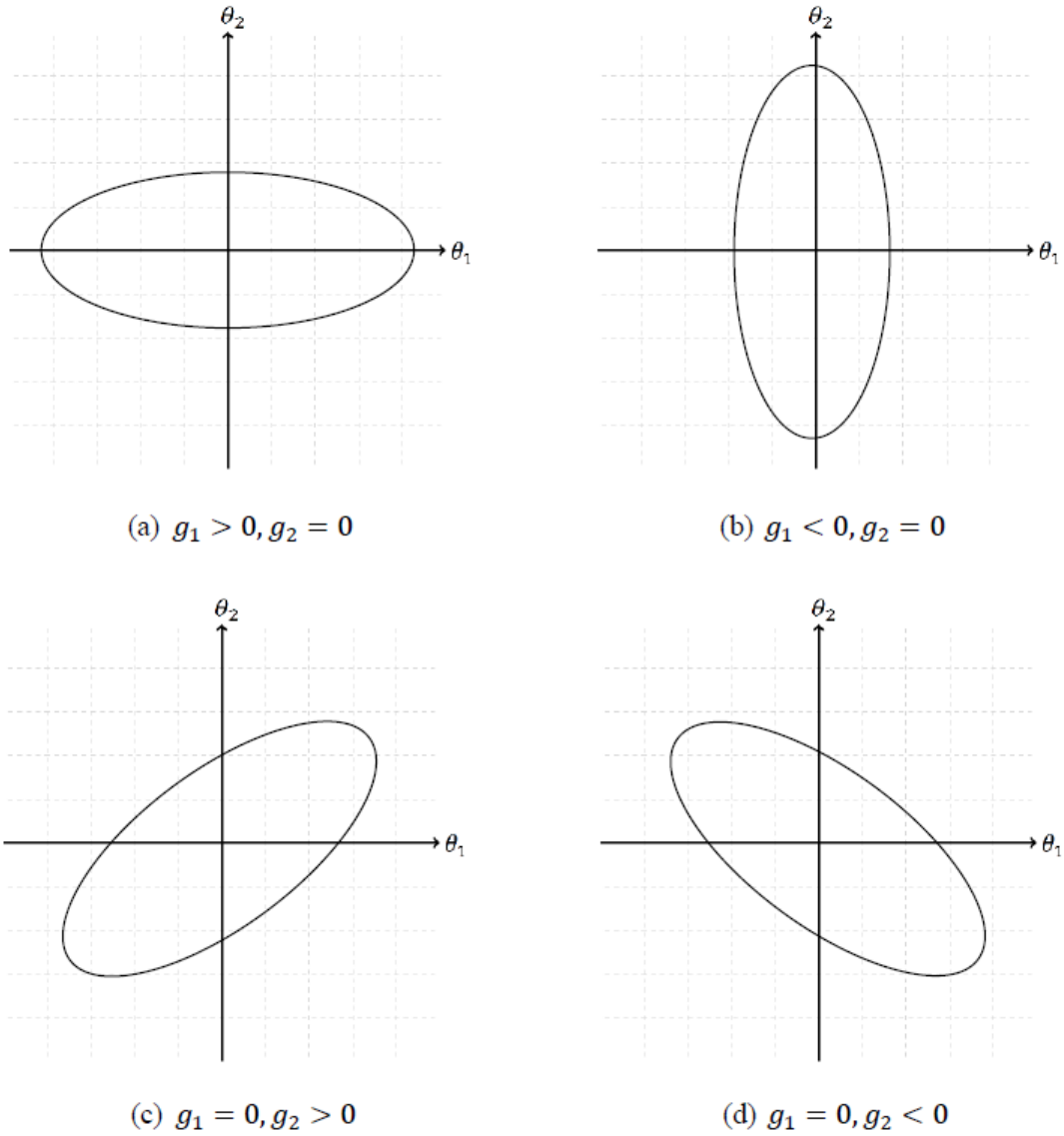

Figure 2.5: Illustration showing the effect of the individual components of the shear. A positive (negative) value of g_1 corresponds to stretching along the lens-plane θ_1 (θ_2) axis. A positive (negative) value of g_2 corresponds to a stretching along the line $\theta_2 = \theta_1$ ($\theta_2 = -\theta_1$).

This angle ϕ tells us about the rotation of the elliptical image. That is, in geometrical terms, the angle between the semi-major axis of the ellipse and the θ_1 axis (Schneider 2005), where a positive angle refers to a counterclockwise rotation. Notice that there is a factor of 2 in the exponent, unlike the ordinary polar form of complex numbers. This is due to the fact that, as mentioned before, g_1 and g_2 are not orthogonal. If you expand (2.30) and plug in, say, $\phi = 45$ degrees, you find that $g_1 = 0$ and the result is shown in Figure 2.5b. Also, for a rotation $\phi =$ 180 degrees, the component g_1 is returned unchanged (rather than negated, as is the case for the normal polar form of complex numbers without the 2). This is due to the rotational symmetry of an ellipse, where a rotation of 180 degrees is the identity transformation.

If we continue with the assumption that our sources are circular with radius R, we can define the semi-major and semi-minor axes of the distorted image as

$$a = \frac{R}{(1-\kappa) - |\gamma|} = \frac{R}{(1-\kappa)(1-|g|)}; b = \frac{R}{(1-\kappa) + |\gamma|} = \frac{R}{(1-\kappa)(1+|g|)}. \tag{2.31}$$

If we then take the ratio of these and simplify we obtain (SWK, p.273)

$$\frac{a}{b} = \frac{1+|g|}{1-|g|}. \tag{2.32}$$

This means that if we have a collection of circular sources we can determine the shear present in the images simply by measuring the semi-major and -minor axes. In practice, however, things are not so simple. Distortions are small and thus the accuracy is greatly dependent on atmospheric seeing conditions, and imperfections in the imaging equipment induce distortions of their own into the images. Even if we discount these problems, the result obtained above rests on the assumption that the sources are circular. However, there is no reason to think that this would be true. The ellipticity present in galaxy images in fact contains contributions

both from shear and from intrinsic ellipticity. Nevertheless there exist methods to extract information about shear from galaxy images, which we turn to next.

2.5.2 Measuring Ellipticity and Shear

In practice, the supply of background galaxies (sources) which we observe are not actually circular objects, but possess some intrinsic ellipticity. Thus, the effect of lensing is either to exaggerate or attenuate this already present ellipticity. (At this point we have not quantitatively defined *ellipticity*, but that is to come. For now, just think of ellipticity as the direction of stretching of the image.) The recipe described above is then useless if applied to a single galaxy image (unless the unadulterated source ellipticity is known). However, if we assume that the source galaxy ellipticity alignments are randomly distrubuted, we can sample over a large number of galaxy images and determine the shear *statistically*. The statistical lensing of sources due to the large scale structure is called *cosmic shear*. Now, if the ellipticity of the source galaxies e^s is randomly distributed, the average over a large number will be 0:

$$\langle e^s \rangle = 0.$$

Let us now revisit the Liouville Theorem mentioned in section 2.4.3. It was stated there that the surface brightness of the source is conserved in lensing, and this resulted in an amplification of the image we see. If we consider small sources so that the convergence and shearl can be assumed constant over the field of view of the image, the lens equation (2.6) can be linearlized to be

$$\boldsymbol{\beta} - \boldsymbol{\beta}(\boldsymbol{\theta_0}) = \boldsymbol{A}(\boldsymbol{\theta_0}) \cdot (\boldsymbol{\theta} - \boldsymbol{\theta_0}), \tag{2.33}$$

and if we write the brightness as a function of $\boldsymbol{\theta}$ as $I(\boldsymbol{\theta})$, then the Liouville Theorem

implies (SWK, p.23)

$$\begin{aligned} I(\boldsymbol{\theta}) &= I^{(s)}(\boldsymbol{\beta}(\boldsymbol{\theta})) \\ &= I^{(s)}(\boldsymbol{\beta}(\boldsymbol{\theta_0}) + \boldsymbol{A}(\boldsymbol{\theta_0}) \cdot (\boldsymbol{\theta} - \boldsymbol{\theta_0})), \end{aligned} \tag{2.34}$$

where the superscript (s) indicates the brightness of the unlensed source.

We can now define the second moments of brightness, a tensor whose components are (SWK, p.274)

$$Q_{ij} = \frac{\int (\theta_i - \bar{\theta}_i)(\theta_j - \bar{\theta}_j) I(\boldsymbol{\theta}) q_I(I(\boldsymbol{\theta})) d^2\theta}{\int I(\boldsymbol{\theta}) q_I(I(\boldsymbol{\theta})) d^2\theta}, \tag{2.35}$$

where $q_I(I(\boldsymbol{\theta}))$ is some filter function. For example, we could choose $q_I(I) = H(I - I_{min})$, where H is the Heaviside step function, so that we only consider regions bounded by isophotes with some minimum threshold intensity. (An *isophote* is a curve composed of points with equal brightness: *iso*=same, *phote*=light.) Also, the $\bar{\theta}_i$ are components of the centroid of the image, which here is defined as

$$\bar{\boldsymbol{\theta}} \equiv \frac{\int \boldsymbol{\theta} I(\boldsymbol{\theta}) q_I(I(\boldsymbol{\theta})) d^2\theta}{\int I(\boldsymbol{\theta}) q_I(I(\boldsymbol{\theta})) d^2\theta}. \tag{2.36}$$

At this point we are finally ready to define precisely what is meant by *ellipticity*. Actually, there is not a single definition of this term in use, so one chooses a definition (or "invents" one) which is convinient. In this case we will choose the complex ellipticity defined as (SWK, p.274)

$$\begin{aligned} \epsilon &\equiv \frac{Q_{11} - Q_{22} + 2iQ_{12}}{Q_{11} + Q_{22} + 2\left(Q_{11}Q_{22} - Q_{12}^2\right)^{1/2}} \\ &= \frac{Q_{11} - Q_{22} + 2iQ_{12}}{\mathrm{Tr}\,\boldsymbol{Q} + 2\sqrt{\det \boldsymbol{Q}}} \end{aligned} \tag{2.37}$$

where in the second line the formula has been shortened a bit, exploiting the fact that the $\boldsymbol{Q}$ matrix is symmetric.

The above definitions apply to the image on the lens plane, but we can also define similar quantities for the unlensed image of the source. For the second moments of brightness we have

$$Q_{ij}^{(s)} = \frac{\int (\beta_i - \bar{\beta}_i)(\beta_j - \bar{\beta}_j) I^{(s)}(\boldsymbol{\beta}) q_I(I^{(s)}(\boldsymbol{\beta})) d^2\beta}{\int I^{(s)}(\boldsymbol{\beta}) q_I(I^{(s)}(\boldsymbol{\beta})) d^2\beta}, \tag{2.38}$$

which is related to the lensed brightness second moment by $\boldsymbol{Q^{(s)}} = \boldsymbol{AQA}$. This can be shown as follows. Recall that the amplification matrix $\boldsymbol{A}$ is the Jacobian matrix for the transformation between coordinates $\boldsymbol{\theta}$ and $\boldsymbol{\beta}$, such that $\boldsymbol{\beta} = \boldsymbol{A\theta}$ and $d^2\beta = \det \boldsymbol{A} d^2\theta$. For convinience we have assumed we have chosen coordinates such that the centroids of the image and source are at their respective origins, so that $\bar{\theta}_{i,j} = 0 = \bar{\beta}_{i,j}$. Taking the $i = j = 1$ component first we have for the source coordinate component

$$\begin{aligned} \beta_1 &= A_{11}\theta_1 + A_{12}\theta_2 \\ &= (1-\kappa)\left[(1-g_1)\,\theta_1 - g_2\theta_2\right] \end{aligned} \tag{2.39}$$

using the definition of the amplification matrix (2.29). For the corresponding second moment of brightness we have then

$$\begin{aligned} Q_{11}^{(s)} &= \frac{\int \beta_1^2 I^{(s)}(\boldsymbol{\beta}) q_I(I^{(s)}(\boldsymbol{\beta})) d^2\beta}{\int I^{(s)}(\boldsymbol{\beta}) q_I(I^{(s)}(\boldsymbol{\beta})) d^2\beta} \\ &= \frac{\int \left[(1-\kappa)\left((1-g_1)\,\theta_1 - g_2\theta_2\right)\right]^2 I(\boldsymbol{\theta}) q_I(I(\boldsymbol{\theta})) d^2\theta}{\int I(\boldsymbol{\theta}) q_I(I(\boldsymbol{\theta})) d^2\theta}, \end{aligned} \tag{2.40}$$

where the Liouville Theorem (2.34) was used to replace the $I^{(s)}(\boldsymbol{\beta})$ with $I(\boldsymbol{\theta})$, the differentials were switched, and the common factor of $\det \boldsymbol{A}$ in the numerator and denominator was cancelled. Now let us write this in a more elucidating way by squaring out the binomial, splitting into separate terms, and pulling out constant

factors from the integrals:

$$Q_{11}^{(s)} = (1-\kappa)^2 \left[(1-g_1)^2 \frac{\int \theta_1^2 I(\boldsymbol{\theta}) q_I(I(\boldsymbol{\theta})) d^2\theta}{\int I(\boldsymbol{\theta}) q_I(I(\boldsymbol{\theta})) d^2\theta} \right.$$
$$-2(1-g_1) g_2 \frac{\int \theta_1\theta_2 I(\boldsymbol{\theta}) q_I(I(\boldsymbol{\theta})) d^2\theta}{\int I(\boldsymbol{\theta}) q_I(I(\boldsymbol{\theta})) d^2\theta} \tag{2.41}$$
$$\left. + g_2^2 \frac{\int \theta_2^2 I(\boldsymbol{\theta}) q_I(I(\boldsymbol{\theta})) d^2\theta}{\int I(\boldsymbol{\theta}) q_I(I(\boldsymbol{\theta})) d^2\theta} \right].$$

Now notice that the fractional factors on the right-most side of each line are actually individual components of the lensed second brightness moment matrix. We can now write $Q_{11}^{(s)}$ simply as

$$Q_{11}^{(s)} = (1-\kappa)^2 \left[(1-g_1)^2 Q_{11} - 2(1-g_1) g_2 Q_{12} + g_2^2 Q_{22} \right]. \tag{2.42}$$

The other two components can be found in a similar way (see Appendix B).

Meanwhile, from the claim that $\boldsymbol{Q^{(s)}} = \boldsymbol{AQA}$ we have

$$\boldsymbol{Q^{(s)}} = (1-\kappa)^2 \begin{bmatrix} 1-g_1 & -g_2 \\ -g_2 & 1+g_1 \end{bmatrix} \begin{bmatrix} Q_{11} & Q_{12} \\ Q_{12} & Q_{22} \end{bmatrix} \begin{bmatrix} 1-g_1 & -g_2 \\ -g_2 & 1+g_1 \end{bmatrix}. \tag{2.43}$$

Carrying out the matrix multiplication, one finds for the $Q_{11}^{(s)}$ component

$$Q_{11}^{(s)} = (1-\kappa)^2 \left[(1-g_1)^2 Q_{11} - 2(1-g_1) g_2 Q_{12} + g_2^2 Q_{22} \right] \tag{2.44}$$

which matches the form found above (and similarly for the other components). Thus $\boldsymbol{Q^{(s)}} = \boldsymbol{AQA}$.

Let us now move forward and use the definition of ellipticity (2.37) to define the *source* ellipticity $\epsilon^{(s)}$, which applies to the unlensed image. It can be related to the lensed ellpiticity and the reduced shear as (SWK, p.275)

$$\epsilon^{(s)} = \begin{cases} \frac{\epsilon - g}{1 - g^*\epsilon} & \text{if } |g| \leq 1 \\ \frac{1 - g\epsilon^*}{\epsilon^* - g^*} & \text{if } |g| > 1 \end{cases}, \tag{2.45}$$

where * denotes the complex conjugate (SWK, p.275).

Now, the quantity that is of actual cosmological interest here is the reduced shear g, not ϵ which is a property of the *image*. It turns out that the expectation value of the ellipticity is an estimator of the reduced shear. To show this, we first invert the relation in (2.45) and then average over the source ellipticity $\epsilon^{(s)}$. For the case of $|g| \leq 1$ the inversion gives

$$\epsilon = \frac{\epsilon^{(s)} + g}{1 + g^* \epsilon^{(s)}}. \tag{2.46}$$

In order to take the expectation value

$$\langle \epsilon \rangle = \int P\left(\epsilon^{(s)}\right) \epsilon d\epsilon^{(s)} \tag{2.47}$$

we first write the source ellipticity as $\epsilon^{(s)} = u\mathrm{e}^{2i\phi} = uv$, so $d\phi = \frac{dv}{2iv}$, and the probability distribution $P(\epsilon^{(s)}) = P(u)P(v)$. Due to statistical isotropy, the angular probability $P(v) = \frac{1}{\pi}$. So we then have for the expectation value

$$\langle \epsilon \rangle = \frac{1}{2\pi i} \int_0^1 \oint_{v(0)}^{v(\pi)} P(u) \frac{uv + g}{1 + g^* uv} \frac{1}{v} dv du. \tag{2.48}$$

Let us start with the v integral. Since the integrand here is a closed contour in the complex plane, we can use the residue theorem to solve the integral. The integrand has two poles, one at $v_1 = 0$ and another at $v_2 = \frac{-1}{g^* u}$, where the denominator will be 0. We see that v_1 lies within our contour (since $v(\phi)$ is a unit circle in the complex plane), but $|v_2| = \frac{1}{|g||u|}$. For our case $|g| \leq 1$, and if we assume also that $u < 1$, then $|v_2| > 1$ which lies outside of the contour. The

integral is then evaluated to be

$$\begin{aligned}\oint f(v)dv &= 2\pi i \,\mathrm{Res}(f(v), v_1) \\ &= 2\pi i \lim_{v\to 0} v f(v) \\ &= 2\pi i \lim_{v\to 0} \frac{uv+g}{1+g^* uv} \\ &= 2\pi i g.\end{aligned} \tag{2.49}$$

This result is independent of u, so the u integral is just $\int_0^1 P(u) = 1$ by normalization. Putting it all together, the factors of $2\pi i$ cancel and we are left with

$$\langle \epsilon \rangle = g; |g| \leq 1 \tag{2.50}$$

for the expectation value of the image ellipticity (Seitz and Schneider 1997). This simple relation provides us with an unbiased esimator for the reduced shear. Furthermore, in the weak lensing regime we have that $\kappa \ll 1$ and $|\gamma| \ll 1$, so that $g \approx \gamma$ (SWK, p.276). Our measured ellipticity in this case, then, provides us with a measurement of the shear itself (and not just the *reduced* shear). The result for the $|g| > 1$ case is equally simple (see Appendix C for the proof):

$$\langle \epsilon \rangle = \frac{1}{g^*}; |g| > 1. \tag{2.51}$$

2.5.3 Tangential and Cross Components of Shear

It is often useful to consider the shear in a rotated reference frame. If we consider a direction ϕ measured relative to the θ_1 axis (with the counterclockwise direction being positive, as usual) then we define the *tangential* and *cross* components of the shear as (SWK, p.277)

$$\begin{aligned}\gamma_t &= -\Re\left[\gamma \mathrm{e}^{-2i\phi}\right] \\ \gamma_\times &= -\Im\left[\gamma \mathrm{e}^{-2i\phi}\right]\end{aligned} \tag{2.52}$$

such that (Kurki-Suonio 2017)

$$\gamma_t = -\gamma_1 \cos 2\phi - \gamma_2 \sin 2\phi \tag{2.53}$$

and

$$\gamma_\times = \gamma_1 \sin 2\phi - \gamma_2 \cos 2\phi. \tag{2.54}$$

Shear is a polar quantity, which is the reason for the presence of the factor of 2 in the exponent. Also take note of the "-" signs in (2.52). These are included to make the component naming more intuitive. If we consider the direction simply along the θ_1 axis (that is, $\phi = 0$) where the shear is real and *positive*, then the stretching will be *along* the θ_1 axis (see Figure 2.5). In this case we intuitively expect the tantential component to be negative, which is thus accomplished with the "-" sign in the γ_t definition above. Similar reasoning holds for a negative real shear component. These relations also hold for the ellipticity ϵ as well.

2.5.4 E- and B-Modes

Thus far the discussion has been focussed on relations among the *actual* values of various quantities. That is, we have not considered *errors* associated with measurement. Without this error, the shear field is subject to certain contraints, and we will begin by looking at what those are. First define a vector field $\boldsymbol{u}_\gamma(\boldsymbol{\theta})$ as (Kurki-Suonio 2017)

$$\boldsymbol{u}_\gamma(\boldsymbol{\theta}) \equiv \nabla\kappa = \begin{bmatrix} \gamma_{1,1} + \gamma_{2,2} \\ \gamma_{2,1} - \gamma_{1,2} \end{bmatrix}. \tag{2.55}$$

This can be shown easily using the definitions of κ and γ in terms of the lensing potential derivatives ψ_{ij}. The derivatives of the shear components are:

$$\begin{aligned}
\gamma_{1,1} &= \frac{\partial \gamma_1}{\partial \theta_1} = \frac{1}{2}\left(\psi_{,111} - \psi_{,122}\right) \\
\gamma_{1,2} &= \frac{\partial \gamma_1}{\partial \theta_2} = \frac{1}{2}\left(\psi_{,112} - \psi_{,222}\right) \\
\gamma_{2,1} &= \frac{\partial \gamma_2}{\partial \theta_1} = \psi_{,112} \\
\gamma_{2,2} &= \frac{\partial \gamma_2}{\partial \theta_2} = \psi_{,122}.
\end{aligned} \tag{2.56}$$

Now for the first component of $\nabla\kappa$ we have

$$\begin{aligned}
\frac{\partial \kappa}{\partial \theta_1} &= \frac{1}{2}\frac{\partial}{\partial \theta_1}\left(\psi_{,11} + \psi_{,22}\right) \\
&= \frac{1}{2}\psi_{,111} + \frac{1}{2}\psi_{,122} \\
&= \underbrace{\frac{1}{2}\psi_{,111} - \frac{1}{2}\psi_{,122}}_{\gamma_{1,1}} + \underbrace{\psi_{,122}}_{\gamma_{2,2}},
\end{aligned} \tag{2.57}$$

and for the second component

$$\begin{aligned}
\frac{\partial \kappa}{\partial \theta_2} &= \frac{1}{2}\frac{\partial}{\partial \theta_2}\left(\psi_{,11} + \psi_{,22}\right) \\
&= \frac{1}{2}\psi_{,112} + \frac{1}{2}\psi_{,222} \\
&= \underbrace{\psi_{,112}}_{\gamma_{2,1}} - \underbrace{\left(\frac{1}{2}\psi_{,112} - \frac{1}{2}\psi_{,222}\right)}_{\gamma_{1,2}}.
\end{aligned} \tag{2.58}$$

Finally, taking the divergence and curl of the vector field we have

$$\nabla \cdot \boldsymbol{u}_\gamma = \nabla^2 \kappa \tag{2.59}$$

and

$$\begin{aligned}
\nabla \times \boldsymbol{u}_\gamma &= \nabla \times \nabla \kappa \\
&= 0,
\end{aligned} \tag{2.60}$$

which are the contraints the shear field satisfies in the absense of error or higher-order effects. However, the *measured* shear may contain error (statistical or systematic) or higher-order effects, and will then not necessarily satisfy thise constraints. One way to handle this is by adding a term to the lensing potential as (SWK, p.372)

$$\psi = \psi^E + i\psi^B. \tag{2.61}$$

The "E-mode" in the above is the potential we have been previously working with, and the "B-mode" is the new term making the lensing potential complex. Note that this definition means that $\boldsymbol{u}_\gamma \neq \nabla\kappa$, so the constraints no longer hold. For the measured shear we have

$$\begin{aligned}\gamma &= \frac{1}{2}\left(\psi_{,11} - \psi_{,22}\right) + i\psi_{,12} \\ &= \underbrace{\frac{1}{2}\left(\psi^E_{,11} - \psi^E_{,22}\right) - \psi^B_{,12}}_{\gamma_1} + i\underbrace{\left[\psi^E_{,12} + \frac{1}{2}\left(\psi^B_{,11} - \psi^B_{,22}\right)\right]}_{\gamma_2}\end{aligned} \tag{2.62}$$

and for the convergence

$$\begin{aligned}\kappa &= \frac{1}{2}\nabla^2\psi = \frac{1}{2}\nabla^2\psi^E + i\frac{1}{2}\nabla^2\psi^B \\ &= \kappa^E + i\kappa^B.\end{aligned} \tag{2.63}$$

As for the potential, the superscript "E" denotes the convergence κ from before, and κ^B is defined by the equation above. For the divergence and curl of $\boldsymbol{u}_\gamma(\boldsymbol{\theta})$ we find (see Appendix D for proof) (SWK, p.372)

$$\nabla \cdot \boldsymbol{u}_\gamma = \nabla^2\kappa^E \tag{2.64}$$

and

$$\nabla \times \boldsymbol{u}_\gamma = \nabla^2\kappa^B. \tag{2.65}$$

Notice that the divergence equation is very similar to the one from earlier, with the convergence swapped out for its corresponding *E-mode*. Thus the E-mode of

the shear is the one which satisfies the contraints in (2.59) and (2.60), and has the properties we expect of the shear. The B-mode, on the other hand, will satisfy $\nabla \cdot \boldsymbol{u}_\gamma = 0$ and quantifies the error in the measurement of the shear. For an illustration of the distinction bewteen the E- and B-modes of the shear, see Figure 2.6 below.

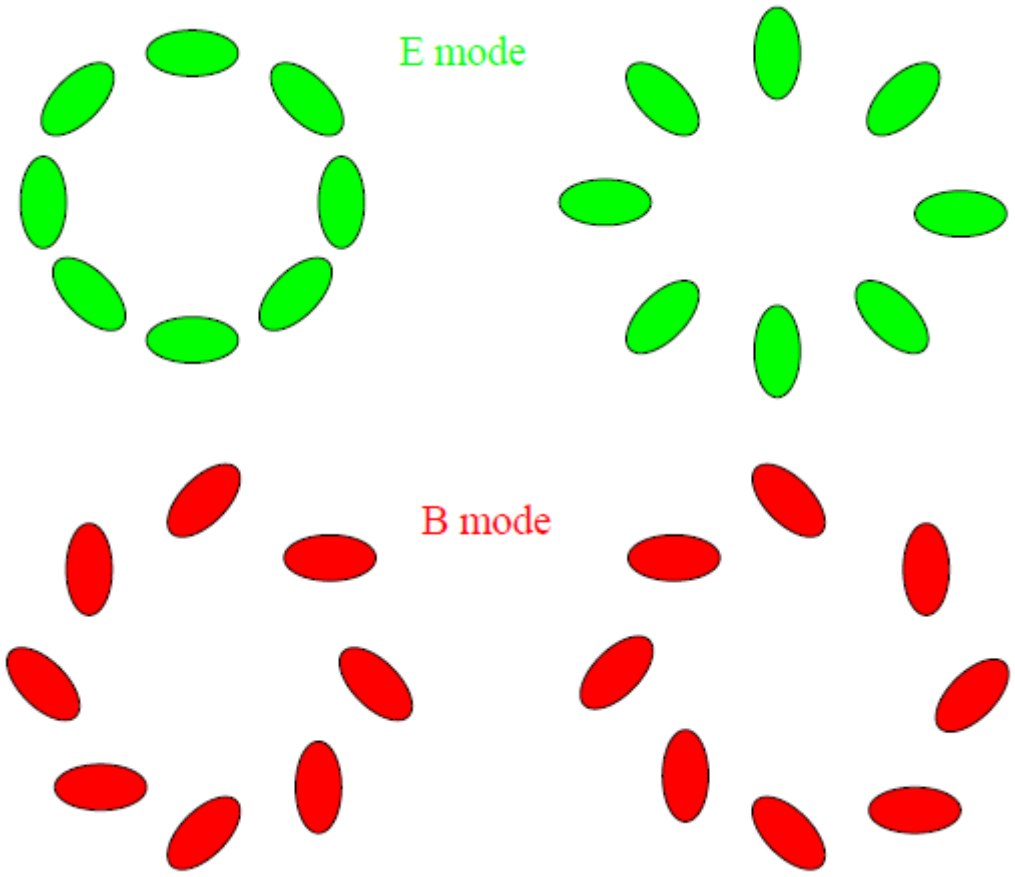

Figure 2.6: (Figure 13 of Van Waerbeke and Mellier (2003)) Illustration showing the distinction between the E- and B-modes. On the top left is shown a shear pattern produced from an *overdensity*, and on the top right one produced from an *underdensity*. The B-modes, however, cannot be produced from gravitational lensing.

Chapter 3

Cosmological Lensing

In our discussion so far, the lens has been treated as some relatively compact distorting mass which was located at some single distance from the observer. However, when one looks out into the universe, the entire matter distribution along the line of sight acts as a lens. In this chapter we expand on the lensing theory presented previously, moving into the realm of cosmological lensing (or, *cosmic shear*), under the flat-sky approximation. In general what we must now do is to *integrate* along the line of sight so that we can include lensing contrubitions from the whole inhomogeneous matter distribution.

3.1 Inversion of Shear in terms of Convergence

One method for obtaining the surface mass density from the shear was developed by Kaiser and Squires (1993). In the following treatise the notation will differ significantly from theirs, and we will obtain the convergence as a function of the

shear. This is necessary since observations of weak gravitational lensing can only give us the reduced shear.

Beginning from the lensing potential (2.20)

$$\psi(\boldsymbol{\theta}) = \frac{1}{\pi}\int \kappa(\boldsymbol{\theta'}) \ln|\boldsymbol{\theta} - \boldsymbol{\theta'}| d^2\theta', \tag{3.1}$$

and the relations between γ_i and ψ

$$\gamma_1(\boldsymbol{\theta}) = \frac{1}{2}\left(\frac{\partial^2\psi}{\partial\theta_1^2} - \frac{\partial^2\psi}{\partial\theta_2^2}\right) \tag{3.2}$$

and

$$\gamma_2(\boldsymbol{\theta}) = \frac{\partial^2\psi}{\partial\theta_1\partial\theta_2}, \tag{3.3}$$

we find the shear $\gamma(\boldsymbol{\theta}) = \gamma_1 + i\gamma_2$ by first evaluating the individual components. First,

$$\begin{aligned}\gamma_1(\boldsymbol{\theta}) =& \frac{1}{2}\left[\frac{1}{\pi}\int \frac{-(\theta_1-\theta_1')^2 + (\theta_2-\theta_2')^2}{|\boldsymbol{\theta}-\boldsymbol{\theta'}|^4}\kappa(\boldsymbol{\theta'})d^2\theta'\right.\\ &\left. - \frac{1}{\pi}\int \frac{-(\theta_2-\theta_2')^2 + (\theta_1-\theta_1')^2}{|\boldsymbol{\theta}-\boldsymbol{\theta'}|^4}\kappa(\boldsymbol{\theta'})d^2\theta'\right]\\ =& \frac{1}{\pi}\int \frac{-(\theta_1-\theta_1')^2 + (\theta_2-\theta_2')^2}{|\boldsymbol{\theta}-\boldsymbol{\theta'}|^4}\kappa(\boldsymbol{\theta'})d^2\theta',\end{aligned} \tag{3.4}$$

where the identity (A.4) has been used. Then for the second component we have

$$\gamma_2(\boldsymbol{\theta}) = \frac{1}{\pi}\int \frac{-2(\theta_1-\theta_1')(\theta_2-\theta_2')}{|\boldsymbol{\theta}-\boldsymbol{\theta}|^4}\kappa(\boldsymbol{\theta'})d^2\theta' \tag{3.5}$$

using (A.8). Combining the components as $\gamma(\boldsymbol{\theta}) = \gamma_1(\boldsymbol{\theta}) + i\gamma_2(\boldsymbol{\theta})$ we get

$$\begin{aligned}\gamma(\boldsymbol{\theta}) &= \frac{1}{\pi}\int \left[\frac{-(\theta_1-\theta_1')^2 + (\theta_2-\theta_2')^2}{|\boldsymbol{\theta}-\boldsymbol{\theta'}|^4} - \frac{2(\theta_1-\theta_1')(\theta_2-\theta_2')}{|\boldsymbol{\theta}-\boldsymbol{\theta'}|^4}\right]\kappa(\boldsymbol{\theta'})d^2\theta'\\ &= \frac{1}{\pi}\int \left[\frac{-(\theta_1-\theta_1')^2 + (\theta_2-\theta_2')^2 - 2i\theta_1\theta_2}{|\boldsymbol{\theta}-\boldsymbol{\theta'}|^4}\right]\kappa(\boldsymbol{\theta'})d^2\theta'.\end{aligned} \tag{3.6}$$

Defining the kernel in the above convolution with $\kappa(\boldsymbol{\theta'})$ to be $D(\boldsymbol{\theta}-\boldsymbol{\theta'})$, we obtain

$$\gamma(\boldsymbol{\theta}) = \frac{1}{\pi}\int D(\boldsymbol{\theta}-\boldsymbol{\theta'})\kappa(\theta')d^2\theta'. \tag{3.7}$$

Now, we will take the equation in (3.7) into Fourier space. For a function $\gamma(\boldsymbol{\theta})$ we use the transform

$$\tilde{\gamma}(\boldsymbol{l}) = \int \gamma(\boldsymbol{\theta}) \mathrm{e}^{-i\boldsymbol{l}\cdot\boldsymbol{\theta}} d^2\theta, \tag{3.8}$$

so (3.7) becomes

$$\tilde{\gamma}(\boldsymbol{l}) = \frac{1}{\pi} \int\int D(\boldsymbol{\theta}-\boldsymbol{\theta'}) \kappa(\boldsymbol{\theta'}) \mathrm{e}^{-i\boldsymbol{l}\cdot\boldsymbol{\theta}} d^2\theta d^2\theta'. \tag{3.9}$$

Now we write $\boldsymbol{u} = \boldsymbol{\theta} - \boldsymbol{\theta'} \rightarrow \boldsymbol{\theta} = \boldsymbol{u} + \boldsymbol{\theta'}$ and $d^2u = d^2\theta$, so

$$\begin{aligned}
\tilde{\gamma}(\boldsymbol{l}) &= \frac{1}{\pi} \int\int D(\boldsymbol{u}) \kappa(\boldsymbol{\theta'}) \mathrm{e}^{-i\boldsymbol{l}\cdot(\boldsymbol{u}+\boldsymbol{\theta'})} d^2u d^2\theta' \\
&= \frac{1}{\pi} \int D(\boldsymbol{u}) \mathrm{e}^{-i\boldsymbol{l}\cdot\boldsymbol{u}} d^2u \int \kappa(\boldsymbol{\theta'}) \mathrm{e}^{-i\boldsymbol{l}\cdot\boldsymbol{\theta'}} d^2\theta' \\
&= \frac{1}{\pi} \tilde{D}(\boldsymbol{l}) \tilde{\kappa}(\boldsymbol{l})
\end{aligned} \tag{3.10}$$

using the definition of the Fourier transform (3.8). Note that the above only holds for $l \neq 0$. Now, we need the above equation solved for $\tilde{\kappa}(\boldsymbol{l})$. First let us perform the above operation in another way. Note that the ∇ operator in Fourier space becomes $i\boldsymbol{l}$, so $\nabla^2 = -l^2$ and for the derivatives of a single component $\frac{\partial^2}{\partial x_i^2} = -l_i^2$. The convergence and shear then transform like

$$\begin{aligned}
\gamma_1(\boldsymbol{\theta}) &= \frac{1}{2}\left(\frac{\partial^2\psi}{\partial\theta_1^2} - \frac{\partial^2\psi}{\partial\theta_2^2}\right) \Rightarrow \tilde{\gamma}_1(\boldsymbol{l}) = -\frac{1}{2}\left(l_1^2 - l_2^2\right)\tilde{\psi}(\boldsymbol{l}), \\
\gamma_2(\boldsymbol{\theta}) &= \frac{\partial^2\psi}{\partial\theta_1\partial\theta_2} \Rightarrow \tilde{\gamma}_2(\boldsymbol{l}) = -l_1 l_2 \tilde{\psi}(\boldsymbol{l}),
\end{aligned}$$

and

$$\kappa(\boldsymbol{\theta}) = \frac{1}{2}\nabla^2\psi(\boldsymbol{\theta}) \Rightarrow \tilde{\kappa}(\boldsymbol{l}) = -\frac{1}{2} l^2 \tilde{\psi}(\boldsymbol{l}).$$

Now $\tilde{\gamma}(\boldsymbol{l}) = \tilde{\gamma}_1(\boldsymbol{l}) + i\tilde{\gamma}_2(\boldsymbol{l})$, so

$$\begin{aligned}
\tilde{\gamma}(\boldsymbol{l}) &= -\frac{1}{2}\left(l_1^2 - l_2^2 + 2il_1l_2\right)\tilde{\psi}(\boldsymbol{l}) \\
&= \frac{1}{\pi}\left[\pi\frac{l_1^2 - l_2^2 + 2il_1l_2}{l^2}\right]\left[-\frac{1}{2}l^2\tilde{\psi}(\boldsymbol{l})\right],
\end{aligned} \tag{3.11}$$

where in the last step we multipled and divided by π (and l^2) and moved the location of the $-1/2$ factor. Now noticing that the factor on the end is actually $\tilde{\kappa}(\boldsymbol{l})$ and comparing to (3.10), we see that evidently

$$\tilde{D}(\boldsymbol{l}) = \pi \frac{l_1^2 - l_2^2 + 2il_1l_2}{l^2}. \tag{3.12}$$

Note that $l^2 = l_1^2 + l_2^2$. If we now multiply $\tilde{D}(\boldsymbol{l})$ with its complex conjugate we get

$$\begin{aligned}
\tilde{D}(\boldsymbol{l})\tilde{D}^*(\boldsymbol{l}) &= \pi^2 \left[\frac{l_1^2 - l_2^2 + 2il_1l_2}{l^2}\right]\left[\frac{l_1^2 - l_2^2 - 2il_1l_2}{l^2}\right] \\
&= \pi^2 \frac{l_1^4 + l_2^4 + 4l_1^2l_2^2 - 2l_1^2l_2^2}{l^4} \\
&= \pi^2 \frac{\left(l_1^2 + l_2^2\right)^2}{l^4} = \pi^2 \frac{l^4}{l^4} \\
&= \pi^2.
\end{aligned} \tag{3.13}$$

If we now multiply both sides of (3.10) by $\tilde{D}^*(\boldsymbol{l})$ we easily find that $\tilde{\kappa}(\boldsymbol{l}) = \frac{1}{\pi}\tilde{D}^*(\boldsymbol{l})\tilde{\gamma}(\boldsymbol{l})$, again for $l \neq 0$. To find the convergence in real space we must perform an inverse Fourier transform:

$$\kappa(\boldsymbol{\theta}) = \frac{1}{(2\pi)^2}\int \tilde{\kappa}(\boldsymbol{l})\mathrm{e}^{i\boldsymbol{l}\cdot\boldsymbol{\theta}}d^2l. \tag{3.14}$$

Applying the above we find

$$\begin{aligned}
\kappa(\boldsymbol{\theta}) =& \frac{1}{(2\pi)^2}\frac{1}{\pi}\int \tilde{D}^*(\boldsymbol{l})\tilde{\gamma}(\boldsymbol{l})\mathrm{e}^{i\boldsymbol{l}\cdot\boldsymbol{\theta}}d^2l \\
=& \frac{1}{(2\pi)^2}\frac{1}{\pi}\int \left[\int D^*(\boldsymbol{\theta''})\mathrm{e}^{-i\boldsymbol{l}\cdot\boldsymbol{\theta''}}d^2\theta'' \right. \\
& \left. \times \int \gamma(\boldsymbol{\theta'})\mathrm{e}^{-i\boldsymbol{l}\cdot\boldsymbol{\theta'}}d^2\theta'\right]\mathrm{e}^{i\boldsymbol{l}\cdot\boldsymbol{\theta}}d^2l \\
=& \frac{1}{(2\pi)^2}\frac{1}{\pi}\int D^*(\boldsymbol{\theta''})d^2\theta'' \\
& \times \int \gamma(\boldsymbol{\theta'})d^2\theta' \int \mathrm{e}^{i\boldsymbol{l}\cdot(\boldsymbol{\theta}-\boldsymbol{\theta''}-\boldsymbol{\theta'})}d^2l.
\end{aligned} \tag{3.15}$$

Now performing the integral over l using the *orthogonality relation*

$$\int \mathrm{e}^{i\boldsymbol{x}\cdot(\boldsymbol{y'}-\boldsymbol{y})}d^dx = (2\pi)^d\delta_D^d(\boldsymbol{y}-\boldsymbol{y'}) \tag{3.16}$$

with $d = 2$ will give an extra factor of $(2\pi)^2$, so

$$\kappa(\boldsymbol{\theta}) = \frac{1}{\pi} \int \gamma(\boldsymbol{\theta'}) d^2\theta' \int D^*(\boldsymbol{\theta''}) \delta_D^d(\boldsymbol{\theta''} - (\boldsymbol{\theta} - \boldsymbol{\theta'})) d^2\theta''. \tag{3.17}$$

Taking now the θ'' integral forces $\boldsymbol{\theta''} = \boldsymbol{\theta} - \boldsymbol{\theta'}$ and we obtain at last

$$\begin{aligned} \kappa(\boldsymbol{\theta}) &= \kappa_0 + \frac{1}{\pi} \int D^*(\boldsymbol{\theta} - \boldsymbol{\theta'}) \gamma(\boldsymbol{\theta'}) d^2\theta' \\ &= \kappa_0 + \frac{1}{\pi} \int \Re \left[D^*(\boldsymbol{\theta} - \boldsymbol{\theta'}) \gamma(\boldsymbol{\theta'}) \right] d^2\theta' \end{aligned} \tag{3.18}$$

where we have included the constant κ_0 for the mode $l = 0$, since it was excluded in the previous steps. Note that this constant actually leads to the so-called *mass-sheet degeneracy* (see Schneider, Wambganss, and Kochanek (2006)), owing to fact that it cannot be determined by the shear. In the second line we have taken the real part of the integrand, since physically the convergence must be a real quantity. In principle this means that the imaginary part would be 0 anyway; however, noise in the data will produce a non-zero imaginary part.

Now, in reality we of course can not measure the shear on continuous sections of the sky, but rather measure it for discrete points (that is, we measure the shear for individual galaxies), so we must actually perform a sum over these diserete galaxy images rather than integration on the lens plane:

$$\hat{\kappa}(\boldsymbol{\theta}) = \frac{1}{n\pi} \sum_i^m \Re \left[D^*(\boldsymbol{\theta} - \boldsymbol{\theta_i}) \gamma(\boldsymbol{\theta_i}) \right]. \tag{3.19}$$

In the estimator (denoted with a "hat") above, we sum over the background galaxy images where shear is measured, n is the number density of said galaxies, and we have reverted to ignoring the constant κ_0.

3.2 The Density Fluctuation and Convergence Power Spectra, P_δ and P_κ

Now we will define the power spectrum of the convergence in terms of the power spectrum of the density fluctuations. For the convergence we have (Schneider, Wambganss, and Kochanek 2006; Kilbinger 2015)

$$\kappa(\boldsymbol{\theta}) = \frac{3}{2}\frac{H_0^2\Omega_m}{c^2}\int_0^{\chi_{lim}} \frac{g(\chi)f_K(\chi)}{a(\chi)}\delta(f_K(\chi)\boldsymbol{\theta},\chi)d\chi, \tag{3.20}$$

where χ is the comoving distance from the observer, δ is the cosmic density contrast, a is the scale factor, f_K is the comoving angular diameter distance, and $g(\chi)$ is called the *lensing efficiency* defined as

$$g(\chi) = \int_\chi^{\chi_{lim}} n(\chi')\frac{f_K(\chi'-\chi)}{f_K(\chi')}d\chi', \tag{3.21}$$

with $n(\chi)d\chi$ being the redshift distribution of source galaxies. First we need to understand how this arises from (2.18),

$$\kappa(\boldsymbol{\theta}) \equiv \frac{\Sigma(\boldsymbol{\theta})}{\Sigma_{crit}}.$$

In the definition of the critical surface mass density, (2.17), the distances D_S, D_L, and D_{LS} are simply the angular diameter distances to the source, to the lens, and from lens to source. These are replaced with the *comoving* angular diameter distances $f_K(\chi')$, $f_K(\chi)$, and $f_K(\chi'-\chi)$, respectively, to account for the expansion of the universe. The function f_K is defined for three cases,

$$f_K(\chi) = \begin{cases} K^{-1/2}\sin(K^{1/2}\chi) & , K > 0 \\ \chi & , K = 0\,, \\ |K|^{-1/2}\sinh(|K|^{1/2}\chi) & , K < 0 \end{cases} \tag{3.22}$$

depending on whether the universe is flat ($K = 0$), open ($K < 0$), or closed ($K > 0$) (Kurki-Suonio 2016). In equation (2.13),

$$\Sigma(r_1, r_2) = \int \delta\rho(r_1, r_2, r_3) dr_3,$$

$\delta\rho$ represents a deviation from the average density of the universe-an over- or under-density. This can be written as $\delta\rho = \rho_m \delta$, where δ is the relative density perturbation. We can further write ρ_m as $\rho_{m,0} a^{-3}$ and $\rho_{m,0} = \Omega_m \rho_{c,0}$, where $\rho_{c,0}$ is the *critical density*, and is

$$\rho_{c,0} = \frac{3H_0^2}{8\pi G}. \tag{3.23}$$

The gravitational effect of the average density is taken care of by the Friedmann-Robertson-Walker (FRW) metric (Kurki-Suonio 2016),

$$ds^2 = -dt^2 + a^2(t) \left[\frac{dr^2}{1 - Kr^2} + r^2 d\theta^2 + r^2 \sin^2 \theta d\phi^2 \right], \tag{3.24}$$

so here we need only consider deviations from the average. For the average density at earlier times (when $a \neq 1$), we multiply by a factor of $1/a$. This gives for the convergence

$$\kappa(\boldsymbol{\theta}, \chi) = \frac{3}{2} \frac{H_0^2 \Omega_m}{c^2} \int_0^\chi \frac{f_K(\chi') f_K(\chi - \chi')}{f_K(\chi)} \frac{\delta(f_K(\chi')\boldsymbol{\theta}, \chi')}{a(\chi')} d\chi'. \tag{3.25}$$

Finally, considering the redshift distribution of source galaxies we get

$$\begin{aligned} \kappa(\boldsymbol{\theta}) &= \int n(\chi) \kappa(\boldsymbol{\theta}, \chi) d\chi \\ &= \frac{3}{2} \frac{H_0^2 \Omega_m}{c^2} \int_0^{\chi_{lim}} \int_\chi^{\chi_{lim}} n(\chi') \frac{f_K(\chi) f_K(\chi' - \chi)}{f_K(\chi')} \delta(f_K(\chi)\boldsymbol{\theta}, \chi) d\chi' d\chi. \end{aligned} \tag{3.26}$$

In (3.20) and (3.2), the integrals could in principle extend out to infinity, but in practice the distance to which an observer can see is finite so the integrals are extended instead extended to some finite distance χ_{lim}. Taking now the Fourier

transform of (3.20) we have

$$\begin{aligned}\kappa(\boldsymbol{l}) &= \int \kappa(\boldsymbol{\theta})\mathrm{e}^{-i\boldsymbol{l}\cdot\boldsymbol{\theta}}d\theta \\ &= \frac{3}{2}\frac{H_0^2\Omega_m}{c^2}\int\int \frac{g(\chi)f_K(\chi)}{a(\chi)}\delta(f_K(\chi)\boldsymbol{\theta},\chi)\mathrm{e}^{-il\theta}d\theta d\chi.\end{aligned} \tag{3.27}$$

Now for the θ integral we have simply the density contrast multiplied with $\mathrm{e}^{-il\theta}$. Note that here we have used the flat-sky approximation in treating $\boldsymbol{\theta}$ as a two dimensional vector on the sky. If we write $\boldsymbol{\phi} = f_K\boldsymbol{\theta} \rightarrow d^2\theta = \frac{1}{f_K}d^2\phi$ then we get

$$\begin{aligned}\int \delta(f_K\boldsymbol{\theta},\chi)\mathrm{e}^{-i\boldsymbol{l}\cdot\boldsymbol{\theta}}d^2\theta &= \frac{1}{f_K}\int \delta(\boldsymbol{\phi},\chi)\mathrm{e}^{-i\frac{\boldsymbol{l}}{f_K}\cdot\boldsymbol{\phi}}d^2\phi \\ &= \frac{1}{f_K}\delta(\boldsymbol{k},\chi), \text{where } \boldsymbol{k} = \frac{\boldsymbol{l}}{f_K}.\end{aligned} \tag{3.28}$$

So then

$$\kappa(\boldsymbol{l}) = \frac{3}{2}\frac{H_0^2\Omega_m}{c^2}\int \frac{g(\chi)}{a(\chi)}\delta(\boldsymbol{k},\chi)d\chi. \tag{3.29}$$

Meanwhile, we define a quantity called the *convergence power spectrum* by the two-point correlation of the convergence in Fourier space:

$$\langle\kappa(\boldsymbol{l})\kappa(\boldsymbol{l'})^*\rangle = (2\pi)^2\delta_D(\boldsymbol{l}-\boldsymbol{l'})P_\kappa(l). \tag{3.30}$$

A similar relation can also be made for the density contrast:

$$\langle\delta(\boldsymbol{k})\delta(\boldsymbol{k'})^*\rangle = (2\pi)^2\delta_D(\boldsymbol{k}-\boldsymbol{k'})P_\delta(k). \tag{3.31}$$

In the two equations above, δ_D is the Dirac delta function. If we now apply these definitions to equation (3.29) we get

$$\begin{aligned}\langle\kappa(\boldsymbol{l})\kappa(\boldsymbol{l'})^*\rangle &= \frac{9}{4}\frac{H_0^4\Omega_m^2}{c^4}\int\left[\frac{g(\chi)}{a(\chi)}\right]^2\langle\delta(\boldsymbol{k},\chi)\delta(\boldsymbol{k'},\chi)^*\rangle d\chi \\ \cancel{(2\pi)^2}P_\kappa(l) &= \frac{9}{4}\frac{H_0^4\Omega_m^2}{c^4}\int\left[\frac{g(\chi)}{a(\chi)}\right]^2\cancel{(2\pi)^2}P_\delta(k,\chi)d\chi,\end{aligned} \tag{3.32}$$

or (Schneider et al. 1998; Schneider, Wambganss, and Kochanek 2006; Fu et al. 2014; Kilbinger 2015)

$$P_\kappa(l) = \frac{9}{4}\frac{H_0^4\Omega_m^2}{c^4}\int_0^{\chi_{lim}}\left[\frac{g(\chi)}{a(\chi)}\right]^2 P_\delta\left(\frac{l}{f_K(\chi)},\chi\right)d\chi. \tag{3.33}$$

In addition, we can consider the two-point correlation of the shear, $\langle\gamma(\boldsymbol{l})\gamma(\boldsymbol{l'})^*\rangle$. However, recalling the relation between shear and convergence in Fourier space (3.10)

$$\gamma(\boldsymbol{l}) = \frac{1}{\pi}D(\boldsymbol{l})\kappa(\boldsymbol{l}),$$

this actually yields for the two-point shear correlation

$$\langle\gamma(\boldsymbol{l})\gamma(\boldsymbol{l})^*\rangle = (2\pi)^2\delta_D(\boldsymbol{l}-\boldsymbol{l'})P_\kappa(l), \tag{3.34}$$

which is the same as for the two-point convergence correlation. So, for weak lensing, the power spetra of the shear and convergence are the same (Hu and White 2001; Schneider, Wambganss, and Kochanek 2006). Furthermore, recall from Section 2.5.2 that the shear can be approximated by the reduced shear, g, which is equal to the expectation value of the ellipticity (see also Schneider, Wambganss, and Kochanek (2006)). That is, $\gamma \approx g = \langle\epsilon\rangle$, so we can write

$$\langle\epsilon(\boldsymbol{l})\epsilon(\boldsymbol{l'})\rangle = (2\pi)^2\delta_D(\boldsymbol{l}-\boldsymbol{l'})P_\kappa(l) \tag{3.35}$$

So, we have a way to estimate the convergence power spectrum from cosmic shear data. Beyond this there exist methods to optimize the estimation of the power spectrum (see e.g. Kaiser (1998), Seljak (1998), and Hu and White (2001)).

3.3 Second Order Statistical Measures

The Aperture Mass Dispersion $\langle M_{ap}^2\rangle$: When attempting to invert the relation between image ellipticities and convergence to obtain a map of the surface mass

density in the weak lensing regime (see Section 3.1), we encounter the *mass sheet degeneracy*, which amounts to adding some constant convergence κ_0 to the inverted convergence $\kappa(\theta)$ (Schneider, Wambganss, and Kochanek 2006). It would therefore be useful to have some quantity defined in terms of the convergence, but which will eliminate this degeneracy. Once such quantity is the *aperture mass*, M_{ap}, defined as the convergence convolved with some spacial filter function U. If we further require that $\int \boldsymbol{\phi} U(\boldsymbol{\phi}) d\boldsymbol{\phi} = 0$, then it can also be written in terms of the tangential component of the shear (2.52), such that (Schneider et al. 1998)

$$M_{ap}(\theta) \equiv \int U(\boldsymbol{\phi})\kappa(\boldsymbol{\phi}) d^2\phi = \int Q(\boldsymbol{\phi})\gamma_t(\boldsymbol{\phi}) d^2\phi, \tag{3.36}$$

and we will have eliminated the degeneracy. In the above, the integration extends over a circle of angular radius θ, and $Q(\boldsymbol{\phi})$ is a weight function (SWK, p.363). For the dispersion we have

$$\langle M_{ap}^2(\theta)\rangle = \int U(\boldsymbol{\phi}) d^2\phi \int U(\boldsymbol{\psi})\langle\kappa(\boldsymbol{\phi})\kappa(\boldsymbol{\psi})\rangle d^2\psi. \tag{3.37}$$

Using the fact that the two-point correlation function is the Fourier transform of the power spectrum, Schneider et al. (1998) obtains

$$\langle M_{ap}^2(\theta)\rangle = 2\pi \int_0^\infty l P_\kappa(l) dl \left[\int_0^\theta \boldsymbol{\phi} U(\boldsymbol{\phi}) J_0(l\boldsymbol{\phi}) d\boldsymbol{\phi}\right]^2. \tag{3.38}$$

Using the filter function (Schneider, Wambganss, and Kochanek 2006)

$$U(\phi) = \frac{9}{\pi\theta^2}\left(1 - \frac{\phi^2}{\theta^2}\right)\left(\frac{1}{3} - \frac{\phi^2}{\theta^2}\right), \tag{3.39}$$

the integral in the square brackets in equation (3.38) becomes (Schneider et al. 1998)

$$I_s(l\theta) = \frac{2^s\Gamma(s+3)}{\pi(l\theta)^{-(s+1)}} J_{s+3}(l\theta), \tag{3.40}$$

where the J_n denote Bessel functions. For $s = 1$ this yields (Schneider, Wambganss, and Kochanek 2006)

$$\langle M_{ap}^2(\theta)\rangle = \frac{288}{\pi}\int_0^\infty l P_\kappa(l) \frac{J_4^2(l\theta)}{(l\theta)^4} dl. \tag{3.41}$$

The Shear Correlation Functions, ξ_+ and ξ_-: One can also define what are called the *shear correlation functions*, defined as

$$\xi_\pm = \langle \gamma_t \gamma_t \rangle(\theta) \pm \langle \gamma_\times \gamma_\times \rangle(\theta) \tag{3.42}$$

where γ_t and $\gamma_\times$ are the tangential and cross components of the shear (see Section 2.5.3). In the first term of (3.43), the γ_t are the in particular the tangential shear components of each galaxy in a pair which have separation θ (and likewise for the $\gamma_\times$). Further, from the assumption of statistical isotropy the expectation values do not depend on the direction of the separation, only the distance. The reference direction for each pair of galaxies used is the separation vector between each pair. These functions are related to the convergence power spectrum (3.33) by (Schneider, Wambganss, and Kochanek 2006)

$$\begin{aligned} \xi_+(\theta) &= \int_0^\infty \frac{l}{2\pi} J_0(l\theta) P_\kappa(l) dl \\ \xi_-(\theta) &= \int_0^\infty \frac{l}{2\pi} J_4(l\theta) P_\kappa(l) dl \end{aligned} \tag{3.43}$$

It is also possible to invert these relations to obtain (Schneider, Wambganss, and Kochanek 2006)

$$P_\kappa(l) = 2\pi \int_0^\infty \theta \xi_+(\theta) J_0(l\theta) d\theta = 2\pi \int_0^\infty \theta \xi_-(l\theta) J_4(l\theta) d\theta \tag{3.44}$$

The Shear Dispersion, $\langle |\bar{\gamma}|^2 \rangle$: Finally, there is the *shear dispersion*, defined as

$$\langle |\bar{\gamma}(\theta)|^2 \rangle = \frac{1}{2\pi} \int l P_\kappa(l) W_{th}(l\theta) dl, \tag{3.45}$$

where $\bar{\gamma}$ is the average shear in some aperture with radius θ and $W_{th}(l\theta)$ is the top-hat window function $W_{th}(l\theta) = \frac{4J_1^2(l\theta)}{(l\theta)^2}$ (Schneider, Wambganss, and Kochanek 2006).

The shear and aperture mass dispersions can also be written in terms of the shear correlation functions as (Schneider, Wambganss, and Kochanek 2006)

$$\langle|\bar{\gamma}(\theta)|^2\rangle = \int_0^{2\theta} \frac{\phi}{\theta^2}\xi_+(\phi)S_+\left(\frac{\phi}{\theta}\right)d\phi = \int_0^{2\theta} \frac{\phi}{\theta^2}\xi_-(\phi)S_-\left(\frac{\phi}{\theta}\right)d\phi \tag{3.46}$$

and

$$\langle M_{ap}^2(\theta)\rangle = \int_0^{2\theta} \frac{\phi}{\theta^2}\xi_+(\phi)T_+\left(\frac{\phi}{\theta}\right)d\phi = \int_0^{2\theta} \frac{\phi}{\theta^2}\xi_-(\phi)T_-\left(\frac{\phi}{\theta}\right)d\phi, \tag{3.47}$$

where $S_\pm$ and $T_\pm$ are the functions (Schneider et al. 2002)

$$\begin{aligned}
S_+(x) &= 4\int_0^\infty \frac{J_0(xt)\left[J_1(t)\right]^2}{t}dt \\
&= \frac{1}{\pi}\left[4\arccos\left(\frac{x}{2}\right) - x\sqrt{4-x^2}\right]\mathrm{H}(2-x) \\
S_-(x) &= 4\int_0^\infty \frac{J_4(xt)\left[J_1(t)\right]^2}{t}dt \\
&= \frac{x(6-x^2)\sqrt{4-x^2} - 8(3-x^2)\arcsin(x/2)}{\pi x^4}\mathrm{H}(2-x) + \frac{4(x^2-3)}{x^4}\mathrm{H}(x-2)
\end{aligned} \tag{3.48}$$

and

$$\begin{aligned}
T_+(x) &= 576\int_0^\infty \frac{J_0(xt)\left[J_4(t)\right]^2}{t^3}dt \\
&= \left[\frac{6(2-15x^2)}{5}\left(1 - \frac{2\arcsin(x/2)}{\pi}\right)\right. \\
&\quad \left. + \frac{x\sqrt{4-x^2}}{100\pi}(120 + 2320x^2 - 754x^4 + 132x^6 - 9x^8)\right]\mathrm{H}(2-x) \\
T_-(x) &= 576\int_0^\infty \frac{J_4(xt)\left[J_4(t)\right]^2}{t^3}dt \\
&= \frac{192}{35\pi}x^3\left(1 - \frac{x^2}{4}\right)^{7/2}\mathrm{H}(2-x),
\end{aligned} \tag{3.49}$$

and $\mathrm{H}(x)$ is the Heavyside step function.

Now, in the previous section we saw that we could obtain the convergence power spectrum directly from cosmic shear observations and, in addition, could produce

various predictions for it based on some chosen cosmological model. It may seem, then, that defining these second order statistics is superfluous. In principle once can constrain the cosmological parameters directly from measurements of P_κ and comparing to theoretical predictions. However, there is an advantage to using these additional measures: they separate out the E- and B-modes (recall the E- and B-mode discussion in Section 2.5.4), which can be desirable. For example, $\langle M_{ap}^2 \rangle$ is senstive only to the E-mode, so it is useful in that it eliminates some types of systematic errors (Fu et al. 2014).

Chapter 4

Results

4.1 Estimating $\Sigma(\theta)$, the Surface Mass Density

Now that we have a sufficient coverage of the fundamental aspects of weak gravitational lensing, let us transition to look at some of the applications of this lensing regime to the study of cosmology. The first of these shall be the surface mass density, $\Sigma(\theta)$, which was first encountered in the previous chapter on general gravitational lensing. Recall that this quantity is a property of the deflecting mass. If we can calculate $\Sigma(\theta)$ (or, equivalently, $\kappa(\theta)$), then we will understand more about the physical structure of the lens. In particular, we will have a better understanding of how the total mass of the lens is distributed.

4.1.1 Smoothing of the Data

If we recall from Chapter 2 that, in the weak lensing regime, the shear and *reduced* shear are approximately equal, and the reduced shear can further be estimated as the expectation value of the ellipticity of the galaxy image (Schneider, Wambganss, and Kochanek 2006). The estimator for the convergence can then be written as

$$\hat{\kappa}(\boldsymbol{\theta}) = \frac{1}{n\pi} \sum_{i}^{m} \Re \left[D^*(\boldsymbol{\theta} - \boldsymbol{\theta_i}) \epsilon_i \right] \tag{4.1}$$

such that ϵ_i is the complex ellpticity of each galaxy image i. Now, one may naively think that in order to determine the convergence for a section of the sky, the ellipticities of the background galaxy images in that region can be inserted into the equation above to obtain the result. However, due to the fact that the ellpiticities come from discrete points on the sky, rather than from a continuous distribution, the estimator in (4.1) will give infinite uncertainty (Kaiser and Squires 1993)! To rectify this problem, we need to smooth the data by introducing a weight function which we convolute with our estimator:

$$\hat{\kappa}_s(\boldsymbol{\theta}) = \int W(|\boldsymbol{\theta} - \boldsymbol{\theta'}|) \hat{\kappa}(\boldsymbol{\theta'}) d^2\theta'. \tag{4.2}$$

We have denoted this smoothed estimator with a subscript "s", and the weight (smoothing) function is assumed to be normalized to 1 (that is, $\int W(|\boldsymbol{\theta} - \boldsymbol{\theta'}|) d^2\theta' = 1$).

Additional smoothing techniques have since been developed as well. In particular, one can first find a smoothed shear estimate from (Seitz and Schneider 1995)

$$\hat{\gamma}_s(\boldsymbol{\theta}) = \frac{\sum_i^m W(|\boldsymbol{\theta} - \boldsymbol{\theta_i}|) \epsilon_i}{\sum_i^m W(|\boldsymbol{\theta} - \boldsymbol{\theta_i}|)}. \tag{4.3}$$

This is then insterted into (3.18) to obtain an estimator of the convergence. Even though this recipe does not give exactly the shear smoothed by a weight function

W, if the number of galaxy images is sufficiently large then the deviation is small (Seitz and Schneider 1995; Lombardi and Schneider 2002). The advantage of using such an estimation method is that it takes into account fluctuations in the local number density of the galaxies (Schneider, Wambganss, and Kochanek 2006).

4.1.2 Examples of Mass Reconstructions

Let us now look at some mass maps that have been obtained from data in recent years.

Reconstruction from CFHTLenS: Van Waerbeke et al. (2013) used data from the Canada-France-Hawaii Telescope Lensing Survey (CFHTLenS) (Heymans et al. 2012; Erben et al. 2013) to estimate the projected matter distribution of the large scale structure, following closely the methodology of Kaiser and Squires (1993) using a Gaussian smoothing function (equation (9) of Van Waerbeke et al. (2013)):

$$W(\boldsymbol{\theta}) = \frac{1}{\pi\theta_0^2}\exp\left(-\frac{|\boldsymbol{\theta}|^2}{2\theta_0^2}\right). \tag{4.4}$$

In their analysis the observed region (approximated to be a flat tangent plane) is divided into gridded cells, and the shear in each cell is calculated from the observed ellipticity using the chosen smoothing function. The surface mass density is subsequently calculated. They then compare their mass reconstructions from CFHTLenS lensing data with predictions based on visible matter to determine the extent to which baryonic matter traces the dark matter.

In order to validate the results, lensing inversion was also done on simulated data obtained from replications of the CFHTLenS observing conditions. N-body simulations are used to produce the dark matter distribution which is then populated with galaxies, using noise properties from real data. The galaxies are

placed on the grid, and the shear and convergence are calculated as with the real CFHTLenS data (Van Waerbeke et al. 2013).

To evaluate the reliability of the reconstruction technique, higher-order moments of the convergence for the simulations and from the mock data reconstructions are computed and compared. The moments $\langle \kappa^n \rangle$ are expectation values of κ to a power n, smoothed over some window funciton. In the flat-sky approximation (which we use in this work), the moment $\langle \kappa^2 \rangle$ would be related to the power spectrum $P_\kappa(k)$ through the window function, $W(k)^2$ (Kurki-Suonio 2017). Figure 4.1 shows the comparison of the true (i.e. κ_E) reconstructed and simulated convergence statistics. The de-noising procedure consists of subtracting off a pure noise reconstruction $\langle \kappa^n_{ran} \rangle$ from the observed convergence $\langle \kappa^n_{obs} \rangle$, where n is the order moment (2, 3, 4, or 5). That is, $\langle \kappa^n_E \rangle = \langle \kappa^n_{obs} \rangle - \langle \kappa^n_{ran} \rangle$. The findings indicate that their reconstruction technique produces reliable mass maps.

The convergence statistics for the real CFHTLenS data are also calculated and compared to the (second and third order) statistics obtained using the redshift distribution of galaxies, which they found could be given by (equation (21) of Van Waerbeke et al. (2013))

$$n_S(z) = A\text{exp}\left(-\frac{(z-0.7)^2}{B^2}\right) + C\text{exp}\left(-\frac{(z-1.2)^2}{D^2}\right), \tag{4.5}$$

with $A = 1.50, B = 0.32, C = 0.20$, and $D = 0.46$. The results are shown in Figure 4.2. Their analysis shows the CFHTLenS data is consistent with the predictions for the second- and third- order moments of the convergence.

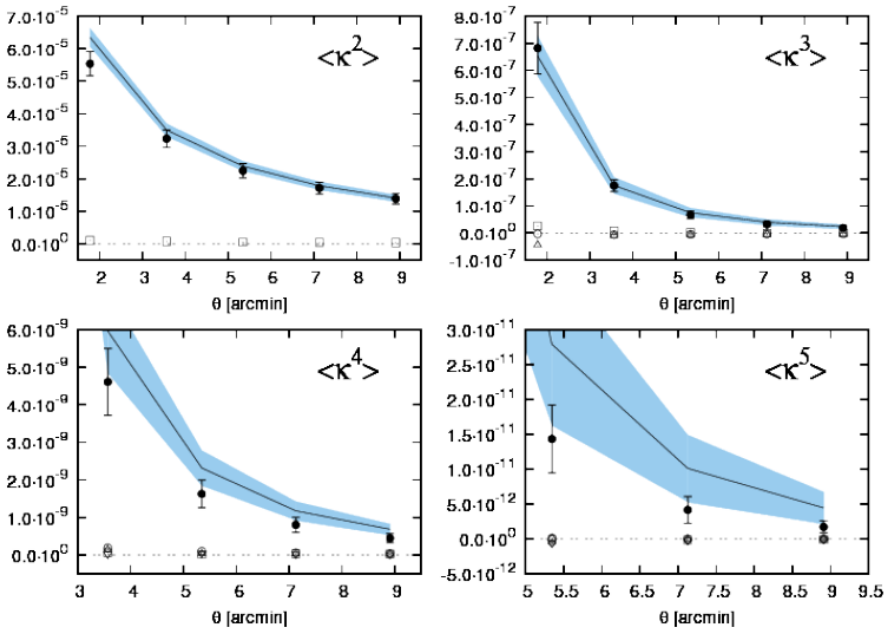

Figure 4.1: (Figure 3 of Van Waerbeke et al. (2013)) The de-noised statistics of the reconstructed data are indicated with black circles (with 1σ deviation error bars), and the simulated statistics are indicated by the solid lines (with 1σ deviation region in blue). See Sections 3 and 4 of their paper for details on the error computation.

Van Waerbeke et al. (2013) proceed to finally construct a mass map using their lensing inversion technique, and compare this to a predicted map based on baryonic content. More specifically, they compared the locations of *extremes* in the predicted map to the reconstructed map. To find the predicted map, each galaxy is assigned a Navarro-Frenk-White dark matter density profile (Navarro, Frenk, and White 1996), and the convergence is predicted based on their redshift. Figures 4.3 and 4.4 depict the peak and trough comparisons, respectively.

From our earlier theoretical discussion of gravitational lensing recall that light from distant objects is lensed due to *all* matter. That is, mass maps constructed from lensing data will provide information on the *total* matter content, both dark

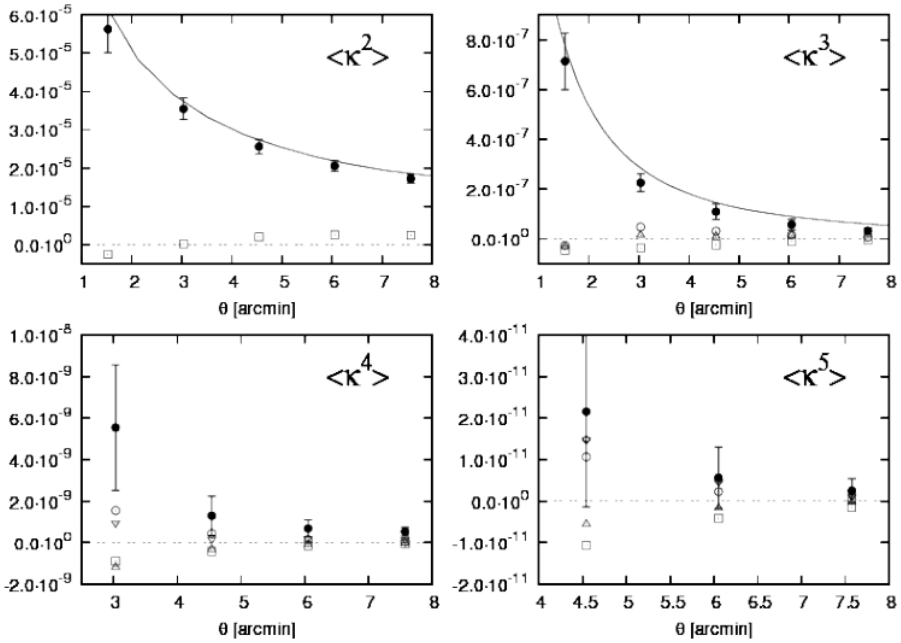

Figure 4.2: (Figure 6 of Van Waerbeke et al. (2013)) The de-noised statistics of the CFHTLenS data are indicated with black circles (with 1σ deviation error bars), and the predicted statistics from redshift distribution are indicated by the solid lines.

and baryonic. What the figures above indicate, then, is that the location of the baryonic (stellar) matter is correllated with the location of the total matter, and evidently the baryonic matter traces the dark matter to at least a first approximation (Van Waerbeke et al. 2013).

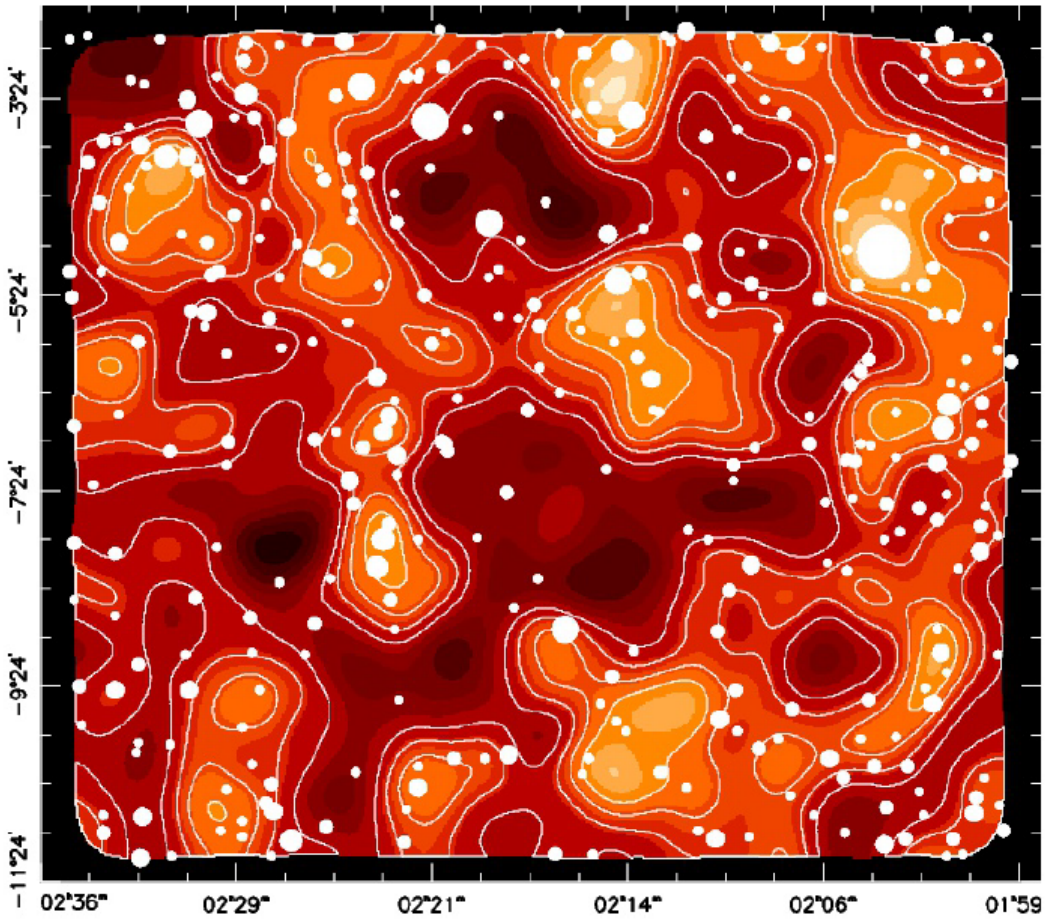

Figure 4.3: (Figure 8 of Van Waerbeke et al. (2013)) The red-orange countour map depicts the mass reconstruction based on lensing inversion of the CFHTLenS data, and the white circles show peaks in the κ map predicted from the redshift distribution. Note that larger circles indicate higher peaks.

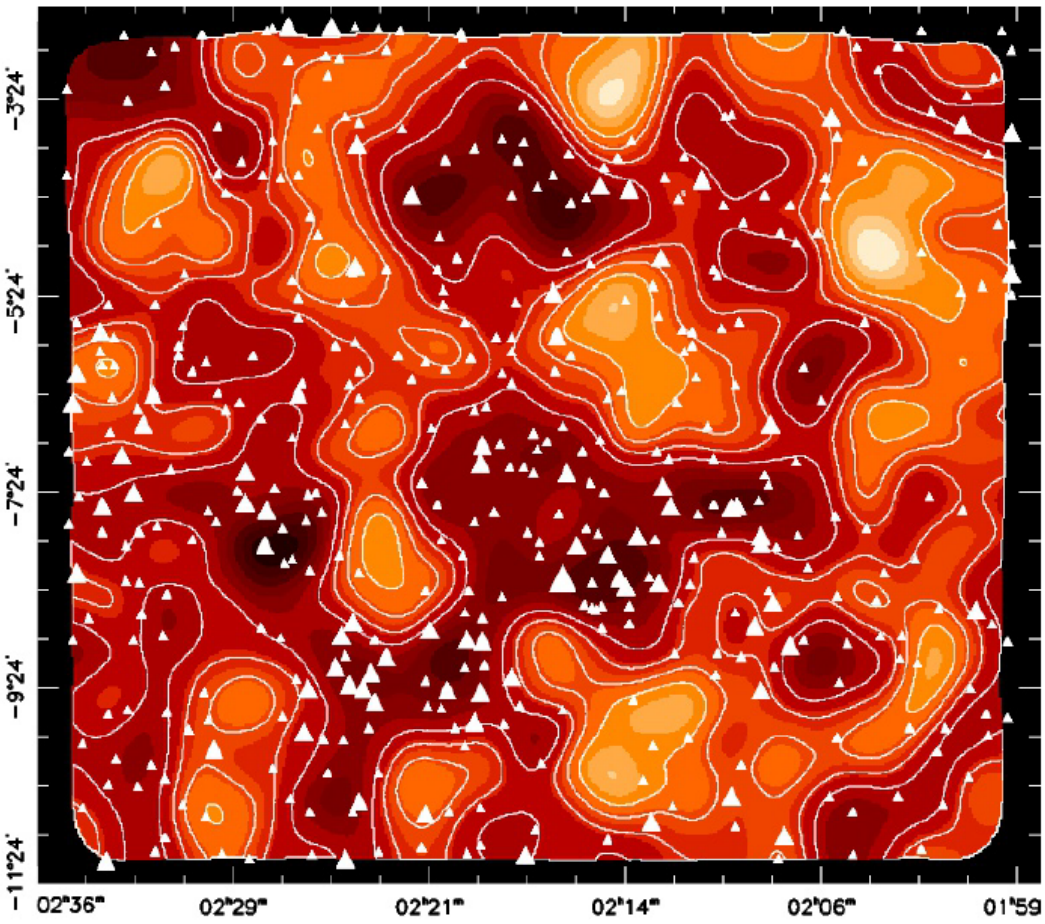

Figure 4.4: (Figure 10 of Van Waerbeke et al. (2013)) The countour map again depicts the mass reconstruction from CFHTLenS. The traingles show locations of troughs in the predicted κ map (again using the redshift distribution).

Reconstruction in the COSMOS Density Field: Another mass reconstruction using weak gravitational lensing done in recent years is that of Amara et al. (2012). In their work, weak lensing data from the Cosmic Evolution Survey (COSMOS) field (Scoville et al. 2007) are used in order to calibrate the density field obtained from various smoothing methods. This is necessary since the statistics of the galaxy distribution and statistics of the dark matter background differ: galaxies form at peaks in the dark matter background, but the mathematical relationship depends on how a *peak* is defined (that is, it depends on what threshold is used to define a peak). For example, the two-point correlaton functions of the galaxies and matter can be related as $\xi_g(r) = b^2\xi_m(r)$, and the factor b is called the *bias*. Amara et al. (2012) calculate the optimal bias for each of their smoothing methos. The authors also reconstruct the mass distribution for each smoothing method, at redshift $z = 1$. These data include galaxy shape measurements from the Hubble Advanced Camera for Surveys (ACS) Imaging, photometric reshifts, and spectroscopic redshifts (see Section 3 of their paper for details).

A fiducial cosmology needed to be assumed in order to relate the redshift to radial distance, so that the expected lensing signal could be calculated. Values for the matter density Ω_m, vacuum energy density Ω_Λ, and Hubble parameter h were chosen to be 0.278, 0.722, and 0.699, respectively. Other cosmological parameters were chosen based on the standard ΛCDM model. Initially the region of interest is divided into a three dimensional grid, and the galaxies are placed into the grid accroding to redshift and angular position. The authors then investigate the effects of four different methods of smoothing: Gaussian, Truncated Singular Isothermal Sphere (TSIS), Nearest-Neighbor (NN), and Multiscale Entropy Filter (MEF). The singular isothermal sphere is a lens model which yields flat rotation curves, as seen in spiral galaxies, with one dimensional velocity dispersion σ (Schneider, Wambganss, and Kochanek 2006). The TSIS model is similar to that of a Gaussian,

except the kernel is modeled by the function $\Sigma(\theta) = \frac{\sigma^2}{\theta} \tan^{-1}\left(\sqrt{\theta_T^2 - \theta^2}/\theta\right)$, where θ_T is the trucation radius and σ is the velocity dispersion of a SIS. In the NN scheme, the density at a point is calculated based on the distance to the fifth nearest neighbor. (Note that in the case of NN, the authors do not use the gridding technique, but instead refer to the one used by Kovač et al. (2010).) They then further segregate the volume based on redshift, investigating the region out to $z < 1$ and to $z < 2$. Now, the shear that is predicted based on the various smoothing methods will be different from the galaxy density field shear. They are related by a factor called the bias, such that $\gamma_i^p = \mu\gamma_i^g$. Here i is either 1 or 2, and the results for each component should be consistent. The optimal bias found for various redshift bins and smoothing methods is given in Figure 4.5 (Table 1 of Amara et al. (2012)). In all smoothing cases the best-fit bias increases for increasing redshift, and the authors conclude that this then must be the case for the underlying galaxy sample.

Smoothing	Bias per slice: $z_{eff} = 0.36$ [$0 < z_s < 1$]	$z_{eff} = 0.70$ [$1 < z_s < 2$]	$z_{eff} = 0.62$ [$0 < z_s < 2$]
Gauss	1.20 ± 0.19	1.85 ± 0.22	1.70 ± 0.17
TSIS	0.99 ± 0.14	1.62 ± 0.18	1.47 ± 0.13
NN	1.59 ± 0.22	2.82 ± 0.34	2.51 ± 0.25
MEF	0.73 ± 0.12	1.34 ± 0.19	1.19 ± 0.13

Figure 4.5: (Table 1 of Amara et al. (2012)) Bias best-fit values for various redshift bins and smoothing methods. The bias increases with redshift for each smoothing method.

Amara et al. (2012) also reconstruct a mass map for the case of $z = 1$, for each of the smoothing methods used. Their results are show in Figure 4.6. A key feature to notice here is that in all cases, the broad features of the mass distribution are captured. The authors note that for the TSIS method, owing to the peaked nature of the lensing kernel, the map contains more small-scale features than do

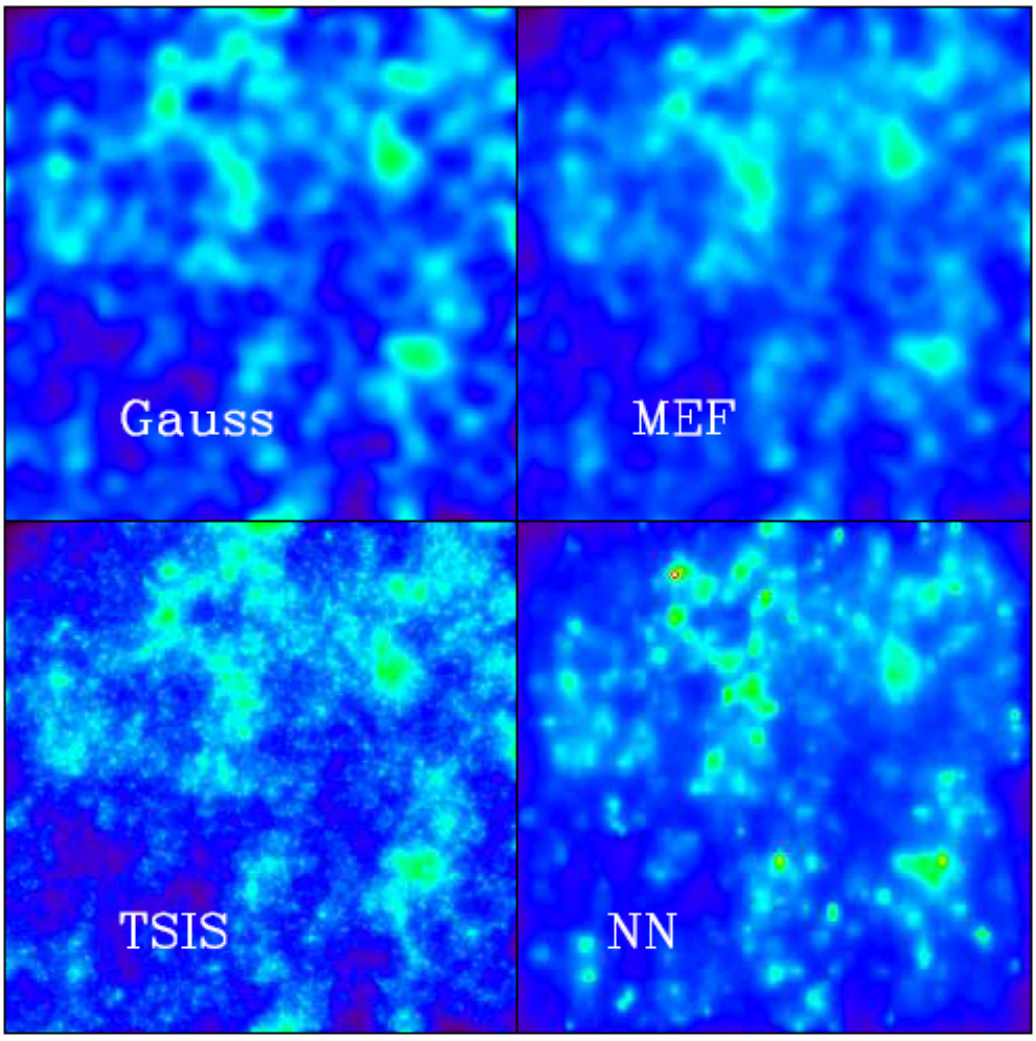

Figure 4.6: (Figure 4 of Amara et al. (2012)) Mass map reconstruction for the various smoothing methods used. Note the higher resolution of the TSIS map, and the presence of higher peaks in the NN map.

the others. Additionally, due to the dynamic nature of the NN smoothing method, the peaks are higher in that reconstruction than in the others.

4.2 Estimating Ω_m and σ_8

As a final application of cosmic shear observations to cosmology we will consider the determination of cosmological parameters. In particular, cosmic shear is most effective in constraining a combination of the matter density parameter (Ω_m) and the power spectrum normalization (σ_8) (and especially their combination, $\sigma_8\Omega_m^\alpha$, where the best exponent value depends on the survey). The matter density parameter is related to the actual matter density by the relation $\Omega_m \equiv \frac{\rho_m}{\rho_c}$, where $\rho_c = \frac{3H^2}{8\pi G}$ is the *critical density*. The quantity σ_8^2 is chosen as the amplitude of the power spectrum of cosmic density fluctuations, and is a measure of the variance in the matter distribution, with a top-hat smoothing scale of $8h^{-1}$ Mpc. It can be assumed that the results presented below are based on the statistical measures shown in the previous chapter, with any exceptions being individually noted.

Fu et al. (2014) measured the aperture mass dispersion from the CFHTLenS (Heymans et al. 2012; Erben et al. 2013) using the estimator (Schneider et al. 2002; Fu et al. 2014)

$$\langle M_{ap,\times}^2(\theta)\rangle = \frac{1}{2}\sum_i \phi_i \Delta\phi_i \left[T_+(\phi_i)\hat{\xi}_+(\phi_i) \pm T_-(\phi_i)\hat{\xi}_-(\phi_i)\right]. \tag{4.6}$$

They then calculated the constraints on the Ω_m-σ_8 combination using two different models for the non-linear power spectrum P_δ. Their results are shown in Table 4.1. In their analysis, the exponent on $\Omega_m/0.27$ was fixed at 0.713. Since the value of Ω_m can be assumed from the data or other cosmological observations, it is common to express the result in terms of a reference value for Ω_m (in this case

0.27), so that the combination $\sigma_8(\Omega_m/0.27)^\alpha$ will straightaway give an idea of the value of σ_8.

Table 4.1: (Table 2 of Fu et al. (2014)) Contraints for the parameter combination $\sigma_8(\Omega_m/0.27)^{0.713}$ from $\langle M_{ap}^2 \rangle$ measured using CFHTLenS data. Two models for the non-linear power spectrum were used and compared: Coyote (Heitmann et al. 2014) and a revised halofit (Takahashi et al. 2012).

Model	$\sigma_8(\Omega_m/0.27)^{0.713}$
Coyote	$0.792^{+0.038}_{-0.045}$
halofit	$0.785^{+0.038}_{-0.045}$

Fu et al. (2014) further compute contraints on this parameter combination by joining the aperture mass dispersion with the third-order aperture mass moment. In particular, they have searched for the value of α which would most tightly constrain the value of $\sigma_8(\Omega_m/0.27)^\alpha$. The *third*-order aperture mass moments are integrals over the *three*-point correlation functions, just as the *second*-order aperture moments are integrals over the *two*-point correlation functions (Fu et al. 2014). Their measures of $\langle M_{ap}^3 \rangle$ incorporate effects of source-lens clustering (where surveyed galaxies actually act as both sources *and* lenses) and intrinsic alignment (where the source ellipticities of galaxies are already aligned to some degree prior to lensing effects) (Fu et al. 2014). The resulting constraints on $\sigma_8(\Omega_m/0.27)^\alpha$ are shown in Table 4.2 for three different cosmological models: flat ΛCDM, flat CDM with dark-energy (wCDM), and curved ΛCDM. Note that the constraints are slightly higher compared to the ones obtained for $\langle M_{ap}^2 \rangle$.

Köhlinger et al. (2016) also compute parameter constraints on the CFHTLenS data. In their analysis, they binned the source galaxies into two redshift bins, and subsequently estimate the shear power spectrum (3.34) directly. In such a *tomographic* analysis, a three dimensional view of the large scale structure can be

Table 4.2: (Table 5 of Fu et al. (2014)) Contraints on $\sigma_8(\Omega_m/0.27)^\alpha$ when combining $\langle M_{ap}^2 \rangle$ with $\langle M_{ap}^3 \rangle$. 68% confidence intervals are given for both the parameter combination and for the exponent.

Parameter	flat ΛCDM	wCDM	curved ΛCDM
$\sigma_8(\Omega_m/0.27)^\alpha$	$0.77^{+0.05}_{-0.07}$	$0.77^{+0.09}_{-0.08}$	$0.79^{+0.07}_{-0.12}$
α	0.64 ± 0.03	0.66 ± 0.02	0.65 ± 0.04

obtained by combining the image "slices". This technique can also allow for the measurement of effects that get projected out in two dimensional lensing (Kilbinger 2015). The analysis was done under the assumption of a flat ΛCDM model. For their baseline calculation, Ω_m, σ_8, h (the Hubble parameter), n_s (the slope of the primordial power spectrum), and Ω_b (the *baryonic* matter density) were taken as free parameters. Köhlinger et al. (2016) also calculate the constraints for a model in which the total neutrino mass, Baryon feedback model amplitude, and systematic redshift bias are also free to vary (the *extended* model). Their results for the parameter combination $\sigma_8(\Omega_m/0.3)^{0.5}$ are given in Table 4.3. It is also plotted in Figure 4.7. In addition, this plot contains the results for this same parameter combination which were obtained from Planck Collaboration et al. (2016). The measurements from Planck probe the universe when it was young (only 380 000 years old) and smooth. Since Planck probes the anisotropies in the cosmic microwave background (CMB), it is a completely different cosmological probe. From the plot you can see that the results of Köhlinger et al. (2016) are consistent with the results from Planck Collaboration et al. (2016).

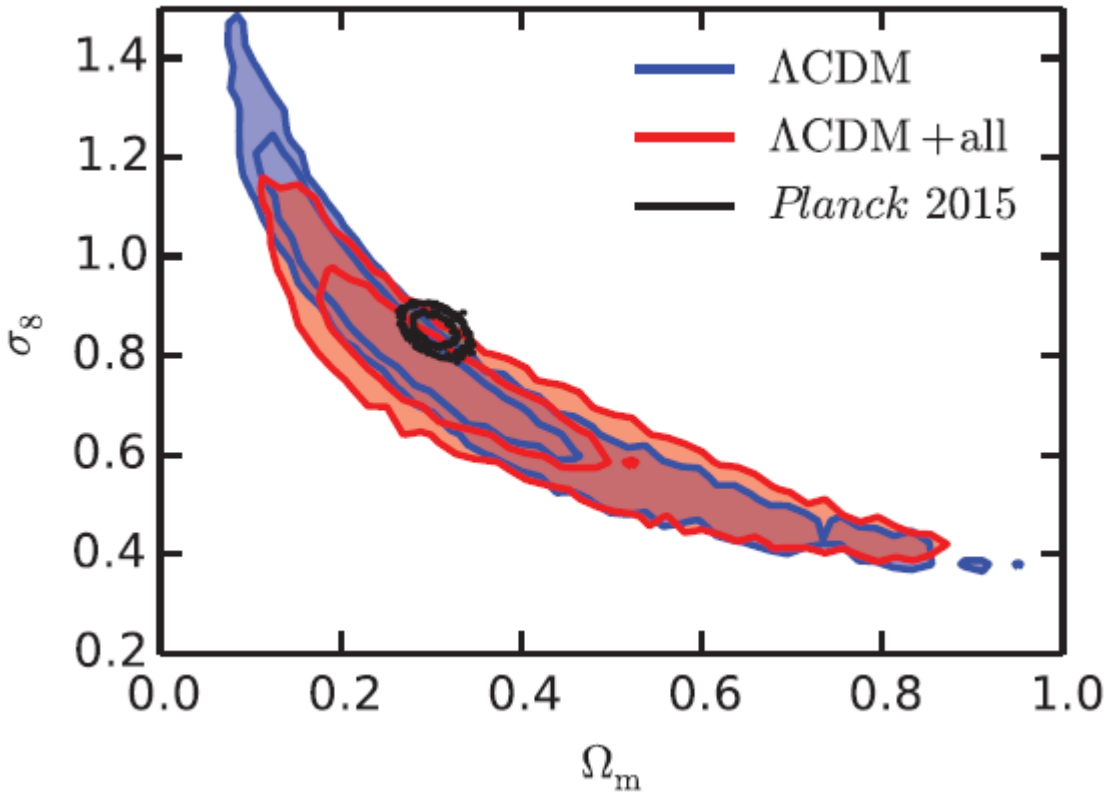

Figure 4.7: (Figure 7 of Köhlinger et al. (2016)) CFHTLenS: Constraints on $\sigma_8(\Omega_m/0.3)^{0.5}$ for the baseline ΛCDM and extended models of Köhlinger et al. (2016), as well as for Planck Collaboration et al. (2016).

Table 4.3: Constraints on $\sigma_8(\Omega_m/0.3)^{0.5}$ for the baseline ΛCDM and extended models of Köhlinger et al. (2016).

Model	$\sigma_8(\Omega_m/0.3)^{0.5}$
ΛCDM	$0.768^{+0.045}_{-0.039}$
ΛCDM extended	$0.755^{+0.059}_{-0.059}$

More recently, we have begun to receive some preliminary results from the Kilo Degree Survey (KiDS) (de Jong et al. 2013) and the Dark Energy Survey (DES) (The Dark Energy Survey Collaboration 2005). Using about 1/3 of the total survey area of KiDS, Hildebrandt et al. (2017) measured the shear correlation functions $\hat{\xi}_+^{ij}$ and $\hat{\xi}_-^{ij}$ from two redshift bins i and j, using the estimators

$$\hat{\xi}_\pm^{ij}(\theta) = \frac{\sum_{a,b} w_a w_b \left[\epsilon_t^i(\boldsymbol{x_a})\epsilon_t^j(\boldsymbol{x_b}) \pm \epsilon_\times^i(\boldsymbol{x_a})\epsilon_\times^j(\boldsymbol{x_b})\right]}{\sum_{a,b} w_a w_b}, \tag{4.7}$$

where the sums are over galaxy pairs a, b and $w_{a,b}$ are the galaxy weights. That is, they obtained the expectation value of the shear correlation (3.42), evaluated as the weighted mean of ellipticity correlations. Using their estimates and the relation between the shear correlation functions and the power spectrum (3.43), they obtain $\sigma_8(\Omega_m/0.3)^{0.5} = 0.745 \pm 0.039$. For this estimate, Hildebrandt et al. (2017) used a flat ΛCDM cosmological model and calibrated the photometric redshift distribution simply using a sample of spectroscopic redshifts. The constraints, plotted in the Ω_m-σ_8 plane can be seen in Figure 4.8. In addition to their results, they present in the same plot the constraints from CFHTLenS, Planck, and pre-Planck work. Hildebrandt et al. (2017) also computed constraints using other redshift calibration techniques (requiring more assumptions-see Section 3 of their paper). These are shown in Figure 4.9.

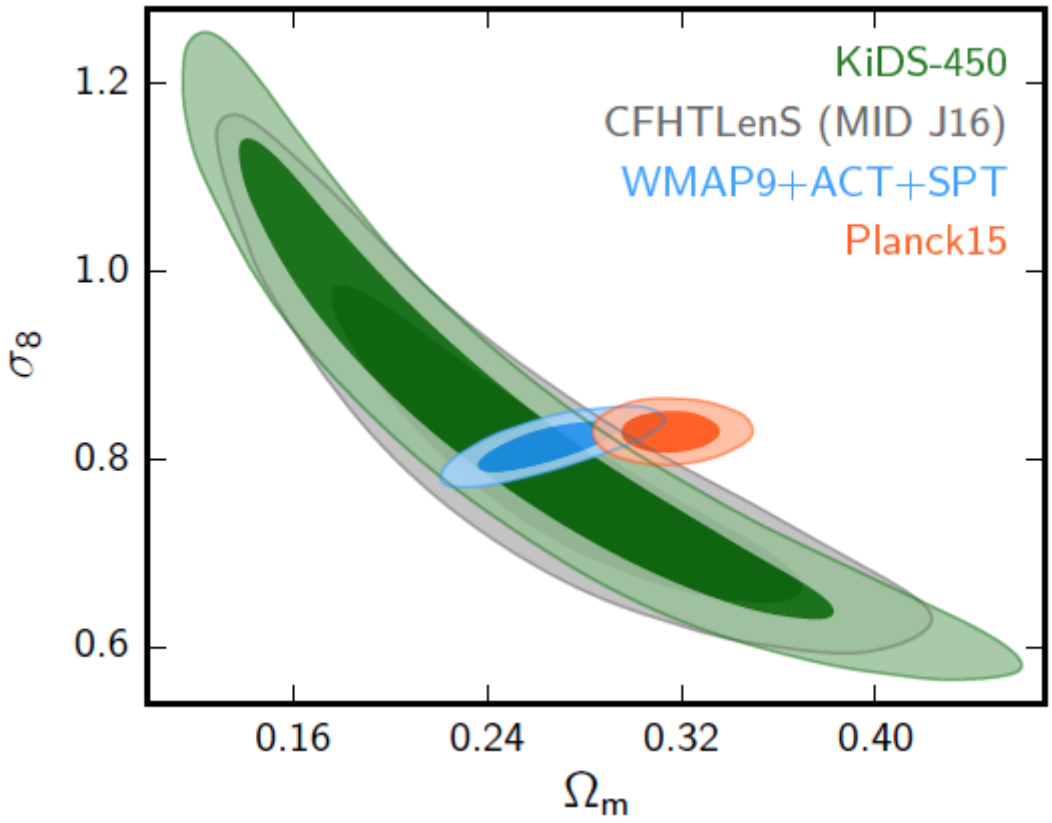

Figure 4.8: (Figure 6a of Hildebrandt et al. (2017)) KiDS: Constraints on Ω_m and σ_8 plotted in the Ω_m-σ_8 plane. Results are shown also from CFHTLenS, Planck, and pre-Planck data.

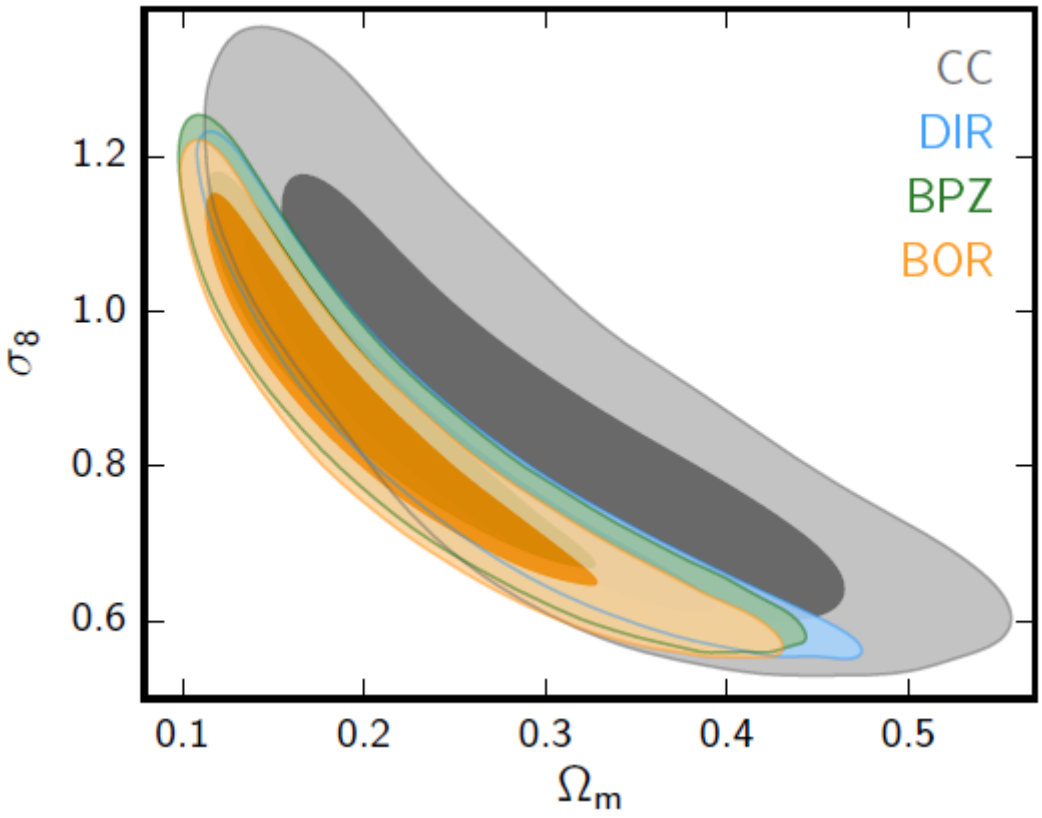

Figure 4.9: (Figure 7 of Hildebrandt et al. (2017)) KiDS: Constraints on Ω_m and σ_8 for the different redshift calibration techniques used. The "weighted direct calibration", DIR, required the fewest assumptions.

Köhlinger et al. (2017) have also analyzed the 450 deg^2 of data currently available from KiDS. In their analysis they binned the source galaxies into two and three redshift bins calculated the shear power spectrum for each. Their resulting constraints on the parameter combination $\sigma_8(\Omega_m/0.3)^{0.5}$ for both redshift bins are given in Table 4.4. Note that these constraints are lower than those obtained by Hildebrandt et al. (2017) using the same data set. However, unlike Hildebrandt et al. (2017), they did not probe the non-linear regime of the power spectrum. In Figure 4.10 are plotted the constraints in the Ω_m-$\sigma_8(\Omega_m/0.3)^{0.5}$ plane for the analyses by both Köhlinger et al. (2017) (for the 2 z-bin case) and Hildebrandt et al. (2017), as well as from Planck Collaboration et al. (2016). In this visualization it is easy to see there is some agreement between the KiDS results presented here, but tension between these and the results from Planck.

Table 4.4: Constraints obtained by Köhlinger et al. (2017) for the parameter combination $\sigma_8(\Omega_m/0.3)^{0.5}$. Results are given for both the 2 and 3 z-bins used in their analysis. Note that the non-linear regime of the shear power spectrum was excluded in their estimation.

z-bin	$\sigma_8(\Omega_m/0.3)^{0.5}$
2	0.624 ± 0.065
3	0.651 ± 0.058

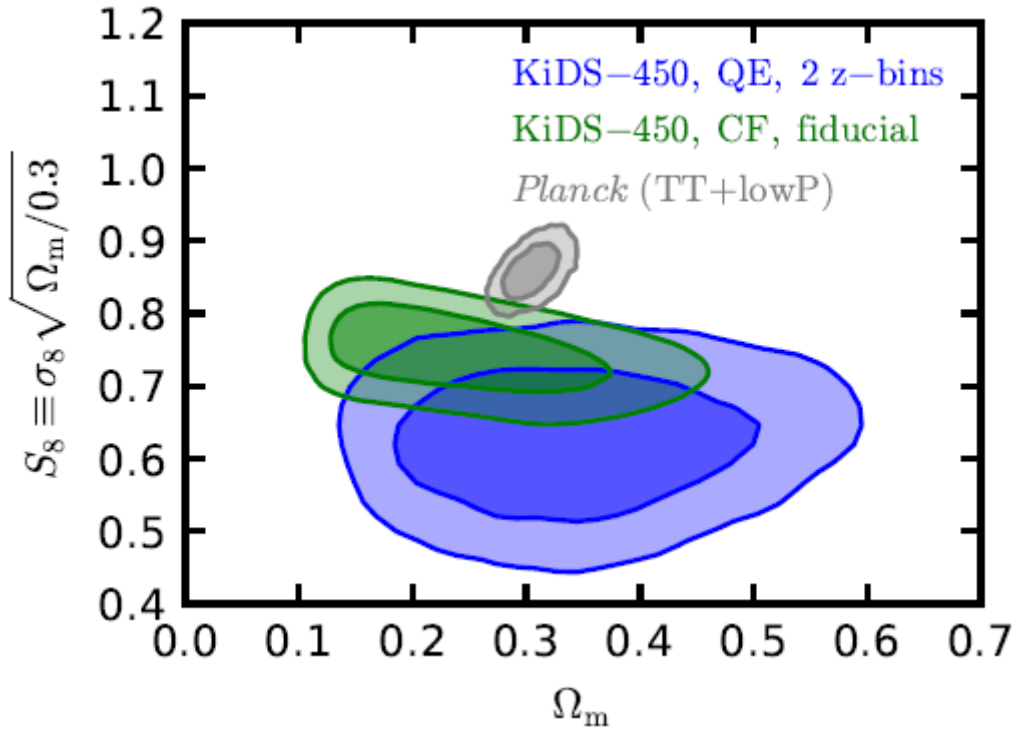

Figure 4.10: (Figure 9a of Köhlinger et al. (2017)) KiDS: Plot showing the results for the constraints on $\sigma_8(\Omega_m/0.3)^{0.5}$. In blue are given the results of the analysis by Köhlinger et al. (2017) for the 2 z-bin case. Results from Hildebrandt et al. (2017) are given in green, and results from Planck Collaboration et al. (2016) are given in grey.

Abbott et al. (2016) performed a three redshift bin tomographic analysis using 139 deg^2 of the Dark Energy Survey, carried out using the Blanco 4-meter at the Cerro Tololo Inter-American Observatory in Chile (The Dark Energy Survey Collaboration 2005). In this preliminary work, the data were used to estimate the shear two-point correlation functions (3.43), and constraints on the parameter combination $\sigma_8(\Omega_m/0.3)^{0.5}$ were subsequently found (Abbott et al. (2016) also found the best fit law for the more general $\sigma_8(\Omega_m/0.3)^{\alpha}$). For the fiducial case ($\alpha = 0.5$) they found $\sigma_8(\Omega_m/0.3)^{0.5} = 0.813^{+0.059}_{-0.060}$. This result is also plotted in Figure 4.11, along with results from Heymans et al. (2013) and Planck Collaboration et al. (2016). As you can see from the figure, these preliminary DES results are consistent with both (separately).

In a more recent analysis, using the first full year of the Dark Energy Survey (DES Y1) covering 1321 deg^2, DES Collaboration et al. (2017) combined measurements of galaxy clustering and galaxy-galaxy lensing with cosmic shear to further constrain the parameters σ_8 and Ω_m. This analysis was performed for both a flat ΛCDM model with 6 free parameters ($\Omega_m, \Omega_b, \Omega_\nu, h, \sigma_8$, and n_s) and a wCDM model with 7 free parameters (those of ΛCDM, plus the dark energy equation of state w). In the case of a flat ΛCDM cosmology, the parameter combination $\sigma_8(\Omega_m/0.3)^{0.5}$ was found to be $0.783^{+0.021}_{-0.025}$, and for Ω_m they found $0.264^{+0.032}_{-0.019}$. For the wCDM model they found $\sigma_8(\Omega_m/0.3)^{0.5} = 0.794^{+0.029}_{-0.027}$ and $\Omega_m = 0.279^{+0.043}_{-0.022}$. The results for the case of the ΛCDM cosmology are depicted in Figure 4.12. In Figure 4.13 we see a plot of $\sigma_8(\Omega_m/0.3)^{0.5}$ versus Ω_m obtained both from these data and from Planck (and their combination).

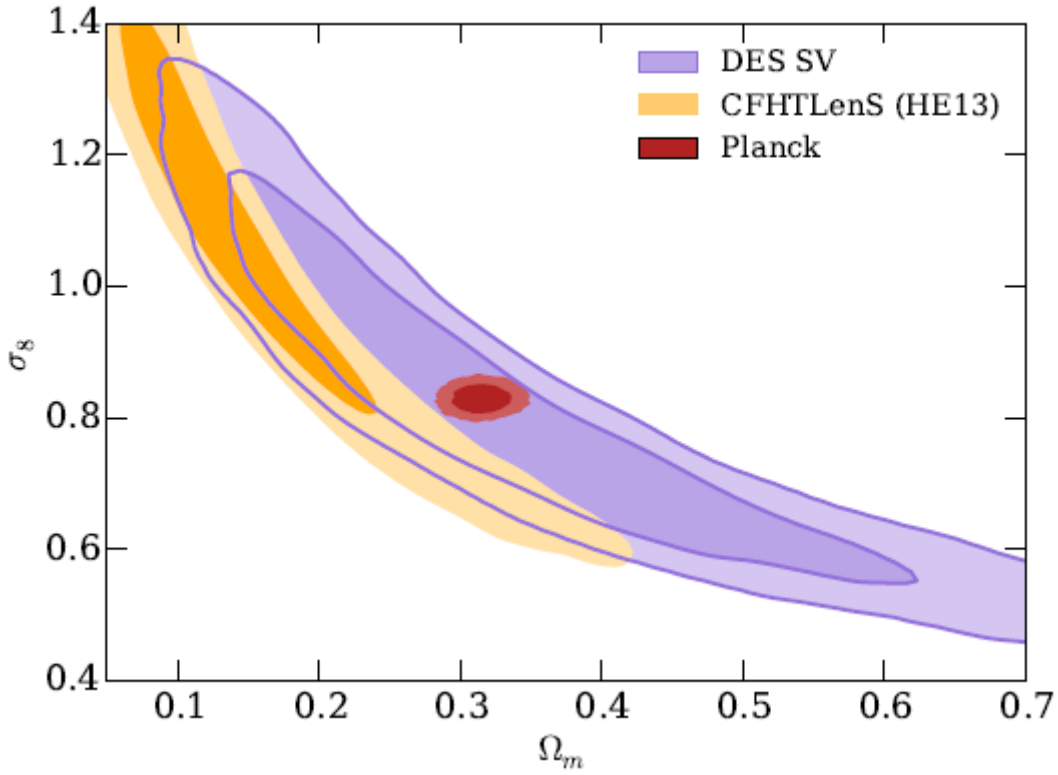

Figure 4.11: (Figure 2 of Abbott et al. (2016)) DES: Plot of $\sigma_8(\Omega_m/0.3)^{0.5}$ in the Ω_m-σ_8 plane for the DES (Abbott et al. 2016), CFHTLenS (Heymans et al. 2013), and Planck (Planck Collaboration et al. 2016) results. For these preliminary DES results, there is apparent consistency with both CFHTLenS and Planck separately.

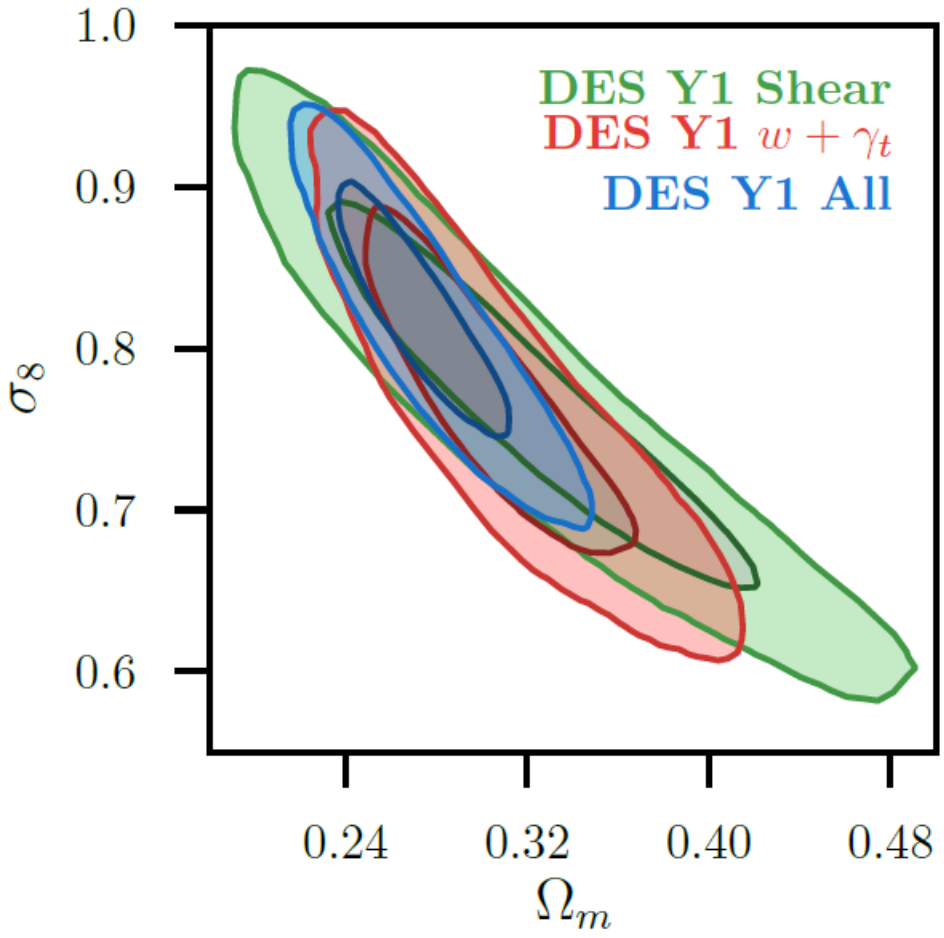

Figure 4.12: (Figure 5 of DES Collaboration et al. (2017)) DES: Plot of $\sigma_8(\Omega_m/0.3)^{0.5}$ in the Ω_m-σ_8 plane for the DES Y1 results (DES Collaboration et al. 2017). In green are the constraints from cosmic shear alone, in red the constraints from galaxy clustering and galaxy-galaxy lensing, and in blue the constraints from a combination of all three. The inner and outer contours represent 68% and 95% confidence levels.

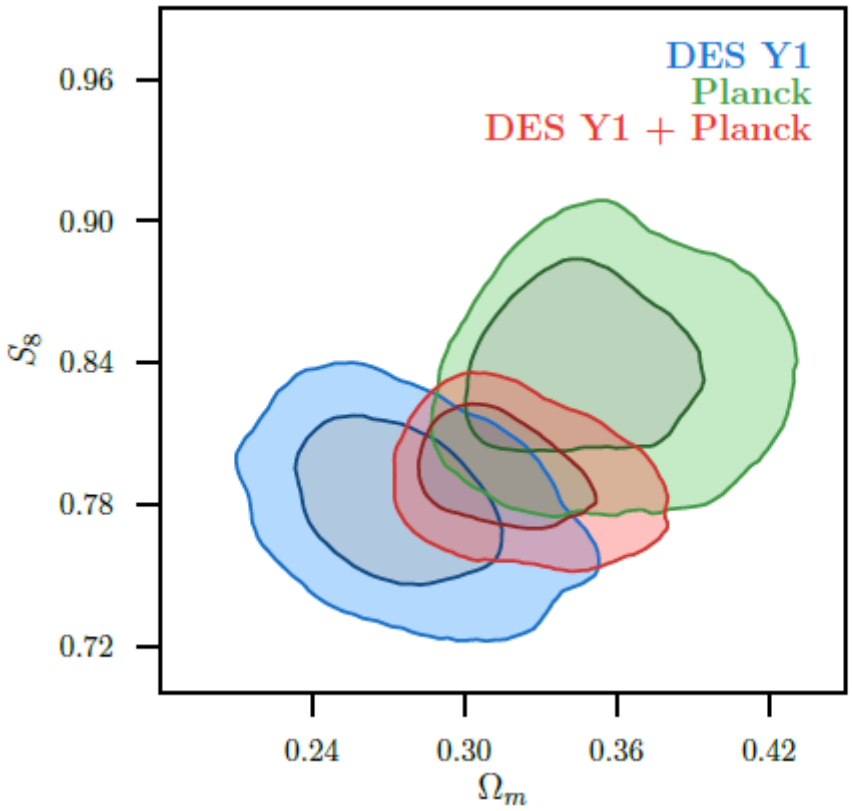

Figure 4.13: (Figure 10 of DES Collaboration et al. (2017)) DES: Plot of $\sigma_8(\Omega_m/0.3)^{0.5}$ for the DES Y1 and Planck, in addition to their combination. DES Collaboration et al. (2017) note that, while visually it may appear that DES and Planck are at odds, they have calculated the Bayes evidence ratio and found that the two sets of results are actually consistent with one another.

Chapter 5

Future of the Field

Our understanding of the cosmos is far from complete, and there is yet much work to be done to understand the nature of large scale structure and parameters which govern the evolution of the unverse. This is in particular true of cosmic shear studies, where we have thus far obtained comsological parameter constraints from just 3 surveys: CFHTLenS, KiDS, and DES, of which the latter 2 are still quite preliminary. The KiDS data is continuing to expand, and will eventually cover 1500 $\deg^2$ of the sky (compared to just the 450 $\deg^2$ used in the work presented above) (de Jong et al. 2013). DES is currently in an even more infantile stage, eventually imaging 5000 $\deg^2$ of the souther sky (The Dark Energy Survey Collaboration 2005). Additionally, in the coming decade we have a few surveys to look forward to which will provide yet more detailed cosmic shear data.

The Large Synoptic Survey Telescope (LSST) is a ground-based, 8.4 meter telescope located in Cerro Pachon, Chile. It will cover 20000 $\deg^2$ of sky over a ten-year period, surveying billions of objects in six color bands. The project is driven by four main science themes: taking an inventory of the solar system,

mapping the Milky Way, exploring the transient optical sky, and probing dark matter and energy. The wide field of view and multi-epoch optical imaging capabilities of the LSST will enable the stacking of weak lensing signals to investigate dark matter halos around galaxies (the survey will also observe strong lensing effects and measure the photometric redshift of 3 billion galaxies). The first light is expected to be collected in 2019, with full science operations beginning in 2021 (LSST Science Collaboration et al. 2009).

The Euclid mission will use a space-based telescope to observe between 15000 and 20000 $\deg^2$ of the sky, with the goal of understanding the acceleration of the Universe and probing the nature of dark matter and energy (*Euclid Consortium Homepage* 2017). This will be done by creating a large-scale structure map covering the last 10 billion years, using measurements of weak graviational lensing and baryonic acoustic oscillations. In particular, for weak lensing Euclid will measure the shapes of 30 galaxies per arcmin^2 (totalling 1.5 billions galaxies by the end of the survey), from which the matter power spectrum can be directly determined. Moreover, the availability of photometric redshifts of the sources will allow for 3 dimensional mapping of the matter distribution. In this way, by determining the dark matter distributioin at different redshifts, Euclid will be able to directly measure the growth of structure in the Universe. Other cosmological information to be obtained from Euclid will be the determination of dark matter density profiles of galaxy clusters by measuring with unprecedented precision the average weak lensing around the clusters, and tightening the constraints on cosmological parameters by complementing the data from Planck. The Euclid satellite is expected to launch in 2020 (Laureijs et al. 2011).

Finally, the Wide Field Infrared Survey Telescope (WFIRST) will be a space-based imaging survey, collecting data for a period of about 6 years. In order to

address questions related to dark matter and energy, the WFIRST will actually conduct 3 types of surveys: High Latitude Spectroscopic Survey, Type Ia Supernovae Survey, and High Latitude Imaging Survey. Of particular relavance to this thesis is the latter, which will use 2400 $\deg^2$ of sky coverage to measure the shapes of distant galaxies and clusters, providing an additional measurement of the growth of large scale structure. It is expected that WFIRST will launch in the mid-2020s (*WFIRST Wide-Field Infrared Telescope Homepage*).

Chapter 6

Conclusions

From Einstein's Theory of General Relativity, it can be shown that light rays will be deflected by the distortions in spacetime caused by the presence of mass. Moreover, since the amount of distortion depends on the distance of the light ray from the deflecting mass, a bundle of light rays will become distorted due to the differential deflection of the different rays in the bundle. Taking only small deflections, we can make a *Born approximation* whereby we treat all the deflections of a light bundle to be additive. It is significant that the mass which is distorting the intervening spacetime is the *total* mass, not just that which is visible to us. This implies that, if we can quantify the amount of distortion in the images which we see, we can understand the quantity and distribution of both the visible and dark matter.

To do this we defined several quantities which carried information about the image distortions. The *convergence* and *shear* described the isotropic size and shape changes, respectively, and these were contained in the *amplification matrix*. For the case of weak gravitational lensing, the amplification matrix was rewritten

in terms of the *reduced shear* which, in the weak regime, could be approximated to equal the shear since the convergence in this case is very small. We were then finally able to define the observable quantity, the *ellipticity*, which quantifies the amount and direction of elongation in galaxy images. We also showed how the ellipticity can be measured using the visible isophotes of the galaxy images. However, because any single galaxy will itself possess some intrinsic amount of ellipticity, it is necessary to observe a large number of galaxy images (whose average intrinsic ellipticity should be zero) so that the shear can be measured statistically. That is, for a given patch of the sky, if the average shear measured in the galaxy images is non-zero then there evidently is some mass in the foreground distorting the light bundles from those galaxies. It is this statistically measured shear which we use to probe the nature of that distorting mass. We ended the second chapter by defining the so called E- and B-modes of shear (and ellipticity). The E-mode is the shear which is actually produced by gravitational lensing, while the B-mode is present due to error (statistical and systematic) and higher-order effects. We further defined the power spetra of the matter density fluctuations and the convergence. In so doing, we also saw that the power spectra of the convergence and of the shear were equal in the weak lensing regime. In addition, we defined several second order statistical measures which were defined in terms of the convergence power spectrum.

Finally, we presented some recent results obtained from cosmic shear observations. In particular, we presented two classes of results: convergence maps (or surface mass density maps) and cosmological parameter constraints. Using the fact that the shear can be estimated by the galaxy image ellipticities, and by inverting the relation between shear and convergence, we presented a method to construct the distribution of foreground mass using observable quantities. Based on the dynamical mass of galaxy clusters and the rotation curves of galaxies, we ascertain

that there must be more mass present in galaxies and clusters than that which is visible to us (van den Bergh 1999). Since gravitational lensing is due to the total mass, not just visible mass, the mass maps created from this inversion process will include this mysterious *dark matter*. We can thus probe the true structure of galaxies and clusters, and determine to what extent the visible matter traces the dark matter. Van Waerbeke et al. (2013) constructed such a mass map using data from CFHTLenS. They validated their findings by applying their inversion procedure to a simulated set of data based on a replication of CFHTLenS oberving conditions. They found that, at least to a first approximation, the baryonic matter distrubition does indeed correlate with the total mass distribution, and is thus a tracer of the dark matter. A reconstruction was also done for the COSMOS Density Field by Amara et al. (2012). In their analysis, they used mass map reconstructions to estimate the optimum *bias*, which relates the two-point correlations of the galaxies and total matter. They found that the optimum bias increases for increasing redshift, at least for redshifts $z < 2$.

The cosmological parameters which tend to best be constrained from cosmic shear are σ_8 (the normalization of the matter power spectrum) and Ω_m (the matter density), and especially their combination $\sigma_8\Omega_m^\alpha$. Using a quantity called the *aperture mass dispersion* (useful, since it separates the E- and B-modes), Fu et al. (2014) calculate constraints using data from CFHTLenS. More precisely, they used two different fitting models for the non-linear matter power spectrum to calculate the constraints on $\sigma_8(\Omega_m/0.27)^{0.713}$. In both cases, they find this parameter combination to be about 0.79. Köhlinger et al. (2016) computed constraints as well for the CFHTLenS data. In their tomographic analysis with two redshift bins and a flat ΛCDM model, they find the parameter combination $\sigma_8(\Omega_m/0.3)^{0.5}$ to be about 0.76, which is in agreement with the data from Planck (Planck Collaboration et al. 2016). More recent results have begun to come in from KiDS

and DES. Using data from KiDS, Hildebrandt et al. (2017) measured the shear correlation functions and, from the relation between these and the power spectrum, calculated $\sigma_8(\Omega_m)^{0.5} \approx 0.74$. This result exhibits some slight tension with the results from Planck (which, remember, determines cosmological parameters from the anisotropy of the cosmic microwave background). Köhlinger et al. (2017) performed a two and three redshift bin tomographic analysis on the same set of KiDS data, finding constraints for ≈ 0.62 and ≈ 0.65, respectively, for the same parameter combination as Hildebrandt et al. (2017). These results are quite in disagreement with the Planck data. However, the results from KiDS are still quite preliminary, and it is premature to draw solid conclusions from the data just yet (they were only using 1/3 of the total survey area). Efstathiou and Lemos (2017) found internal inconsistencies in the KiDS data as analyzed by Hildebrandt et al. (2017), and concluded that more effort is needed to understand these inconsistencies before inferences can be drawn. Furthermore, the disagreement arises when one *assumes* a ΛCDM model. Assuming a different cosmological model may lead to agreement. Using initial data from DES, Abbott et al. (2016) carried out a three redshift tomographic analysis. Estimating the shear correlation functions, they find $\sigma_8(\Omega_m)^{0.5} \approx 0.81$. More recently, DES Collaboration et al. (2017) carried out a *four* redshift bin tomographic analysis on the full first year of DES data, combining cosmic shear measurements with those of galaxy-galaxy lensing and galaxy clustering, to obtain $\sigma_8(\Omega_m)^{0.5} \approx 0.78$. While this result was in good agreement with the Planck results, the data from DES is still quite preliminary at the time of this writing, and solid conclusions should therefore not yet be drawn.

Bibliography

Abbott, T. et al. (2016). "Cosmology from cosmic shear with Dark Energy Survey Science Verification data". In: *Phys. Rev. D* 94.2, p. 022001. arXiv: astro-ph/1507.05552.

Amara, A. et al. (2012). "The COSMOS density field: a reconstruction using both weak lensing and galaxy distributions". In: *MNRAS* 424, pp. 553–563. arXiv: astro-ph/1205.1064.

de Jong, J. T. A. et al. (2013). "The Kilo-Degree Survey". In: *Experimental Astronomy* 35, pp. 25–44. arXiv: astro-ph/1206.1254.

DES Collaboration et al. (2017). "Dark Energy Survey Year 1 Results: Cosmological Constraints from Galaxy Clustering and Weak Lensing". In: arXiv: 1708.01530.

Dyson, F. W., A. S. Eddington, and C. Davidson (1920). "A Determination of the Deflection of Light by the Sun's Gravitational Field, from Observations Made at the Total Eclipse of May 29, 1919". In: *Philosophical Transactions of the Royal Society of London A: Mathematical, Physical and Engineering Sciences* 220.571-581, pp. 291–333. ISSN: 0264-3952.

Efstathiou, G. and P. Lemos (2017). "Problems with KiDS". In: arXiv: 1707.00483.

Einstein, A. (1916). “Die Grundlage der allgemeinen Relativitätstheorie”. In: *Ann. Phys.* 49, pp. 769–822.

Erben, T. et al. (2013). “CFHTLenS: the Canada-France-Hawaii Telescope Lensing Survey - imaging data and catalogue products”. In: *MNRAS* 433, pp. 2545–2563. arXiv: astro-ph/1210.8156.

Euclid Consortium Homepage (2017). URL: http://www.euclid-ec.org/ (visited on 07/17/2017).

Fu, L. et al. (2014). “CFHTLenS: cosmological constraints from a combination of cosmic shear two-point and three-point correlations”. In: *MNRAS* 441, pp. 2725–2743. arXiv: astro-ph/1404.5469.

Heavens, A. (2011). “Cosmology with Gravitational Lensing”. In: arXiv: astro-ph/1109.1121 [astro-ph.CO].

Heitmann, K. et al. (2014). “The Coyote Universe Extended: Precision Emulation of the Matter Power Spectrum”. In: *Astrophys. J.* 780, p. 111.

Heymans, C. et al. (2012). “CFHTLenS: the Canada-France-Hawaii Telescope Lensing Survey”. In: *MNRAS* 427, pp. 146–166. arXiv: astro-ph/1210.0032.

Heymans, C. et al. (2013). “CFHTLenS tomographic weak lensing cosmological parameter constraints: Mitigating the impact of intrinsic galaxy alignments”. In: *MNRAS* 432, pp. 2433–2453. arXiv: astro-ph/1303.1808.

Hildebrandt, H. et al. (2017). “KiDS-450: cosmological parameter constraints from tomographic weak gravitational lensing”. In: *MNRAS* 465, pp. 1454–1498. arXiv: astro-ph/1606.05338.

Hu, W. and M. White (2001). “Power Spectra Estimation for Weak Lensing”. In: *Astrophys. J.* 554, pp. 67–73.

Kaiser, N. (1998). “Weak Lensing and Cosmology”. In: *Astrophys. J.* 498, pp. 26–42.

Kaiser, N. and G. Squires (1993). "Mapping the dark matter with weak gravitational lensing". In: *Astrophys. J.* 404, pp. 441–450.

Kilbinger, M. (2015). "Cosmology with cosmic shear observations: a review". In: *Reports on Progress in Physics* 78.8, 086901, p. 086901. arXiv: astro-ph/1411.0115.

Köhlinger, F. et al. (2016). "A direct measurement of tomographic lensing power spectra from CFHTLenS". In: *MNRAS* 456, pp. 1508–1527. arXiv: astro-ph/1509.04071.

Köhlinger, F. et al. (2017). "KiDS-450: The tomographic weak lensing power spectrum and constraints on cosmological parameters". In: arXiv: astro-ph/1706.02892.

Kovač, K. et al. (2010). "The Density Field of the 10k zCOSMOS Galaxies". In: *Astrophys. J.* 708, pp. 505–533. arXiv: astro-ph/0903.3409 [astro-ph.CO].

Kurki-Suonio, H. (2016). *Cosmology*. URL: www.courses.physics.helsinki.fi/teor/cosmology/.

— (2017). *Galaxy Survey Cosmology*. URL: http://www.courses.physics.helsinki.fi/teor/gsc/.

Laureijs, R. et al. (2011). "Euclid Definition Study Report". In: arXiv: astro-ph/1110.3193 [astro-ph.CO].

Lombardi, M. and P. Schneider (2002). "Smooth maps from clumpy data: Covariance analysis". In: *Astron. Astrophys.* 392. arXiv: astro-ph/0201385.

LSST Science Collaboration et al. (2009). "LSST Science Book, Version 2.0". In: arXiv: astro-ph/0912.0201.

Navarro, J. F., C. S. Frenk, and S. D. M. White (1996). "The Structure of Cold Dark Matter Halos". In: *Astrophys. J.* 462, p. 563. arXiv: astro-ph/9508025.

Planck Collaboration et al. (2016). "Planck 2015 results. XIII. Cosmological parameters". In: *Astron. Astrophys.* 594, A13, A13. arXiv: astro-ph/1502.01589.

Schneider, P. (2005). "Weak Gravitational Lensing". In: arXiv: astro-ph/0509252.

Schneider, P., J. Wambganss, and C. Kochanek (2006). *Gravitational lensing: strong, weak, and micro*. Springer.

Schneider, P. et al. (1998). "A new measure for cosmic shear". In: *MNRAS* 296, pp. 873–892. arXiv: astro-ph/9708143.

Schneider, P. et al. (2002). "Analysis of two-point statistics of cosmic shear. I. Estimators and covariances". In: *Astron. Astrophys.* 396, pp. 1–19. eprint: astro-ph/0206182.

Scoville, N. et al. (2007). "The Cosmic Evolution Survey (COSMOS): Overview". In: *Astrophys. J. Suppl. Ser.* 172, pp. 1–8. arXiv: astro-ph/0612305.

Seitz, C. and P. Schneider (1995). "Steps towards nonlinear cluster inversion through gravitational distortions II. Generalization of the Kaiser and Squires method." In: *Astron. Astrophys.* 297, p. 287. arXiv: astro-ph/9408050.

— (1997). "Steps towards nonlinear cluster inversion through gravitational distortions. III. Including a redshift distribution of the sources." In: 318, pp. 687–699. eprint: astro-ph/9601079.

Seljak, U. (1998). "Weak Lensing Reconstruction and Power Spectrum Estimation: Minimum Variance Methods". In: *Astrophys. J.* 506, pp. 64–79.

Takahashi, R. et al. (2012). "Revising the Halofit Model for the Nonlinear Matter Power Spectrum". In: *Astrophys. J.* 761, 152, p. 152. arXiv: astro-ph/1208.2701.

The Dark Energy Survey Collaboration (2005). "The Dark Energy Survey". In: arXiv: astro-ph/0510346.

van den Bergh, S. (1999). "The Early History of Dark Matter". In: arXiv: astro-ph/9904251.

Van Waerbeke, L. and Y. Mellier (2003). "Gravitational Lensing by Large Scale Structures: A Review". In: arXiv: astro-ph/0305089.

Van Waerbeke, L. et al. (2013). "CFHTLenS: mapping the large-scale structure with gravitational lensing". In: *MNRAS* 433, pp. 3373–3388. arXiv: astro-ph/1303.1806.

Walsh, D., R. F. Carswell, and R. J. Weymann (1979). "0957 + 561 A, B - Twin quasistellar objects or gravitational lens". In: *Nature* 279, pp. 381–384.

WFIRST Wide-Field Infrared Telescope Homepage. URL: https://wfirst.gsfc.nasa.gov/index.html (visited on 07/17/2017).

Appendix A

Logarithm Identities

For some two-dimensional vector $\boldsymbol{q} = q_1\hat{e}_1 + q_2\hat{e}_2$,

$$\begin{aligned}\frac{\partial}{\partial q_1}\ln|\boldsymbol{q}| &= \frac{\partial}{\partial q_1}\ln\sqrt{q_1^2+q_2^2} \\ &= \frac{1}{\sqrt{q_1^2+q_2^2}}\frac{1}{2}\left(q_1^2+q_2^2\right)^{-1/2}2q_1 \\ &= \frac{q_1}{q_1^2+q_2^2}\end{aligned} \tag{A.1}$$

and then

$$\begin{aligned}\frac{\partial^2}{\partial q_1^2}\ln|\boldsymbol{q}| &= \frac{q_1^2+q_2^2-2q_1^2}{\left(q_1^2+q_2^2\right)^2} \\ &= \frac{-q_1^2+q_2^2}{|\boldsymbol{q}|^4}.\end{aligned} \tag{A.2}$$

Likewise,

$$\frac{\partial}{\partial q_2}\ln|\boldsymbol{q}| = \frac{q_2}{q_1^2+q_2^2}; \frac{\partial^2}{\partial q_2^2}\ln|\boldsymbol{q}| = \frac{-q_2^2+q_1^2}{|\boldsymbol{q}|^4}. \tag{A.3}$$

The difference of these is easy:

$$\frac{\partial^2}{\partial q_1^2}\ln|\boldsymbol{q}| - \frac{\partial^2}{\partial q_2^2}\ln|\boldsymbol{q}| = 2\frac{-q_1^2+q_2^2}{|\boldsymbol{q}|^4}. \tag{A.4}$$

For the Laplacian we find

$$\begin{aligned}\nabla^2 \ln|\boldsymbol{q}| &= \frac{\partial^2}{\partial q_1^2}\ln|\boldsymbol{q}| + \frac{\partial^2}{\partial q_2^2}\ln|\boldsymbol{q}| \\ &= 0.\end{aligned} \tag{A.5}$$

However, this holds only if $\boldsymbol{q} \neq \mathbf{0}$. For the case of $\boldsymbol{q} = \mathbf{0}$ we need to do a bit more work. If we consider the integral of the Laplacian above, and apply the divergence theorem, we have

$$\begin{aligned}\int\int_A \nabla^2 \ln|\boldsymbol{q}| dA &= \int\int_A \nabla\cdot\nabla \ln|\boldsymbol{q}| dA \\ &= \int_S \nabla \ln|\boldsymbol{q}|\cdot d\boldsymbol{S} = \int_S \left[\frac{q_1}{q^2}\hat{\boldsymbol{e}}_1 + \frac{q_2}{q^2}\hat{\boldsymbol{e}}_2\right]\cdot d\boldsymbol{S} \\ &= \int_S \frac{\boldsymbol{q}}{q^2} d\boldsymbol{S} = \int_S \frac{q^2}{q^2} d\phi = 2\pi\end{aligned} \tag{A.6}$$

since $d\boldsymbol{S} = \boldsymbol{q} d\phi$, and where we used (A.1) and (A.3). If we now simply *assume* that $\nabla^2 \ln|\boldsymbol{q}| = 2\pi\delta_D(\boldsymbol{q})$ and compute the integral, we indeed find it also equals 2π (or 0 if $\boldsymbol{q} \neq 0$). So,

$$\nabla^2 \ln|\boldsymbol{q}| = 2\pi\delta_D(\boldsymbol{q}). \tag{A.7}$$

Lastly, for the cross component $\frac{\partial^2}{\partial q_1 \partial q_2}\ln|\boldsymbol{q}|$ we have

$$\begin{aligned}\frac{\partial}{\partial q_2}\left[\frac{\partial}{\partial q_1}\ln\sqrt{q_1^2+q_2^2}\right] &= \frac{\partial}{\partial q_2}\left[\frac{q_1}{q_1^2+q_2^2}\right] \\ &= \frac{-2q_1q_2}{(q_1^2+q_2^2)} \\ &= \frac{-2q_1q_2}{q^4}.\end{aligned} \tag{A.8}$$

Appendix B

Source Second Brightness Moments

In a similar fashion, taking the $i = j = 2$ component we have for source second brightness moment

$$Q_{22}^{(s)} = \frac{\int \beta_2^2 I^{(s)}(\boldsymbol{\beta}) q_I(I^{(s)}(\boldsymbol{\beta})) d^2\beta}{\int I^{(s)}(\boldsymbol{\beta}) q_I(I^{(s)}(\boldsymbol{\beta})) d^2\beta} \tag{B.1}$$

and for the source coordinate

$$\begin{aligned} \beta_2 &= A_{12}\theta_1 + A_{22}\theta_2 \\ &= (1-\kappa)\left[-g_2\theta_2 + (1-g_2)\,\theta_2\right]. \end{aligned} \tag{B.2}$$

Then squaring this expression for β_2^2, plugging the result into $Q_{22}^{(s)}$, applying Liouville's Theorem, and writing in separate terms we get

$$\begin{aligned} Q_{22}^{(s)} = (1-\kappa)^2 \Bigg[& g_2^2 \frac{\int \theta_1^2 I(\boldsymbol{\theta}) q_I(I(\boldsymbol{\theta})) d^2\theta}{\int I(\boldsymbol{\theta}) q_I(I(\boldsymbol{\theta})) d^2\theta} \\ & -2\,(1+g_1)\,g_2 \frac{\int \theta_1\theta_2 I(\boldsymbol{\theta}) q_I(I(\boldsymbol{\theta})) d^2\theta}{\int I(\boldsymbol{\theta}) q_I(I(\boldsymbol{\theta})) d^2\theta} \\ & +(1+g_2)^2 \frac{\int \theta_2^2 I(\boldsymbol{\theta}) q_I(I(\boldsymbol{\theta})) d^2\theta}{\int I(\boldsymbol{\theta}) q_I(I(\boldsymbol{\theta})) d^2\theta} \Bigg]. \end{aligned} \tag{B.3}$$

Noticing that the fractional factors are the individual components of the image second brightness moments we see that

$$Q_{22}^{(s)} = (1-\kappa)^2 \left[g_2^2 Q_{11} - 2\,(1+g_1)\, g_2 Q_{12} + (1+g_1)^2\, Q_{22} \right], \tag{B.4}$$

which matches the result of the matrix multiplication in equation (2.43).

Finally for the cross component we take $i = 1$ and $j = 2$ so that

$$Q_{12}^{(s)} = \frac{\int \beta_1 \beta_2 I^{(s)}(\boldsymbol{\beta}) q_I(I^{(s)}(\boldsymbol{\beta})) d^2\beta}{\int I^{(s)}(\boldsymbol{\beta}) q_I(I^{(s)}(\boldsymbol{\beta})) d^2\beta}. \tag{B.5}$$

Making the appropriate substitutions and separating terms gives

$$\begin{aligned} Q_{12}^{(s)} = (1-\kappa)^2 \Bigg[& - g_2\,(1-g_1) \frac{\int \theta_1^2 I(\boldsymbol{\theta}) q_I(I(\boldsymbol{\theta})) d^2\theta}{\int I(\boldsymbol{\theta}) q_I(I(\boldsymbol{\theta})) d^2\theta} \\ & + 2\left(1 - g_1^2 + g_2^2\right) \frac{\int \theta_1 \theta_2 I(\boldsymbol{\theta}) q_I(I(\boldsymbol{\theta})) d^2\theta}{\int I(\boldsymbol{\theta}) q_I(I(\boldsymbol{\theta})) d^2\theta} \\ & - g_2\,(1+g_1) \frac{\int \theta_2^2 I(\boldsymbol{\theta}) q_I(I(\boldsymbol{\theta})) d^2\theta}{\int I(\boldsymbol{\theta}) q_I(I(\boldsymbol{\theta})) d^2\theta} \Bigg]. \end{aligned} \tag{B.6}$$

which again matches the result of the matrix multiplication of equation (2.43).

Appendix C

Source Ellipticity

For the case $|g| > 1$ we have

$$\begin{aligned} \epsilon &= \frac{1 + g\left(\epsilon^{(s)}\right)^*}{\left(\epsilon^{(s)}\right)^* + g^*} \\ &= \frac{1 + guv}{uv + g^*}, \end{aligned} \tag{C.1}$$

letting $\left(\epsilon^{(s)}\right)^* = uv$. Then $d\phi = \frac{dv}{-2vi}$ so the average becomes

$$\langle \epsilon \rangle = \frac{-1}{2\pi i} \int_0^1 \oint_{v(0)}^{v(\pi)} P(u) \frac{1 + guv}{uv + g^*} \frac{1}{v} dv du, \tag{C.2}$$

where the angular probability $P(v) = \frac{1}{\pi}$ from statistical isotropy. The poles for the integrand of the v integral are $v_1 = 0$ and $v_2 = -\frac{g^*}{u}$. The first pole is again inside the contour, but $|v_2| = \frac{|g|}{|u|} > 1$ (since we are treating the $|g| > 1$ case and assume that $|u| < 1$) is outside of the contour. The v integral is then evaluated to

be

$$\begin{aligned}\oint f(v)dv &= -2\pi i \operatorname{Res}(f, v_1) \\ &= -2\pi i \lim_{v\to 0} v f(v) \\ &= -2\pi i \lim_{v\to 0} \frac{1+guv}{uv+g^*} \\ &= \frac{-2\pi i}{g^*},\end{aligned} \tag{C.3}$$

again independent of u. Notice that the prefactor on the residue is negative, since the contour $v = \mathrm{e}^{-2i\phi}$ is this time a *counterclockwise* unit circle in the complex plane. The u integral again evaluates to 1, and putting it all together we find

$$\begin{aligned}\langle \epsilon \rangle &= \left(\frac{-1}{2\pi i}\right)\left(\frac{-2\pi i}{g^*}\right) \\ &= \frac{1}{g^*}.\end{aligned} \tag{C.4}$$

Appendix D

Divergence and Curl of $\boldsymbol{u}_\gamma(\boldsymbol{\theta})$

The shear components are

$$\gamma_1 = \frac{1}{2}\left(\psi^E_{,11} - \psi^E_{,22}\right) - \psi^B_{,12} \tag{D.1}$$

and

$$\gamma_2 = \psi^E_{,12} + \frac{1}{2}\left(\psi^B_{,11} - \psi^B_{,22}\right). \tag{D.2}$$

For the divergence we have

$$\begin{aligned} \nabla \cdot \boldsymbol{u}_\gamma &= \partial_1\left(\gamma_{1,1} + \gamma_{2,2}\right) + \partial_2\left(\gamma_{2,1} - \gamma_{1,2}\right) \\ &= \gamma_{1,11} - \gamma_{1,22} + 2\gamma_{2,12}, \end{aligned} \tag{D.3}$$

where we have used the fact that $\gamma_{i,jk} = \gamma_{i,kj}$, and have shortened the notation by defining $\frac{\partial}{\partial\theta_i}$ as ∂_i. The relevant derivatives of the shear components are

$$\begin{aligned} \gamma_{1,11} &= \frac{1}{2}\left(\psi^E_{,1111} - \psi^E_{,1122}\right) - \psi^B_{,1112} \\ \gamma_{1,22} &= \frac{1}{2}\left(\psi^E_{,1122} - \psi^E_{,2222}\right) - \psi^B_{,1222} \\ \gamma_{2,12} &= \psi^E_{,1122} + \frac{1}{2}\left(\psi^B_{,1112} - \psi^B_{,1222}\right). \end{aligned} \tag{D.4}$$

Now putting it all together we have

$$\begin{aligned}\nabla \cdot \boldsymbol{u}_\gamma &= \frac{1}{2}\left[\psi^E_{,1111} - \psi^E_{,1122} + 4\psi^E_{,1122} - \psi^E_{,1122} + \psi^E_{,2222}\right] - \cancel{\psi^B_{,1112}} + \cancel{\psi^B_{,1112}} - \cancel{\psi^B_{,1222}} + \cancel{\psi^B_{,1222}} \\ &= \frac{1}{2}\left[\psi^E_{,1111} + \psi^E_{,2222} + 2\psi^E_{,1122}\right].\end{aligned} \tag{D.5}$$

This is equal to $\nabla^2\kappa^E$ since

$$\begin{aligned}\nabla^2\kappa^E &= \frac{1}{2}\nabla^2\left[\psi^E_{,11} + \psi^E_{,22}\right] \\ &= \frac{1}{2}\left[\psi^E_{,1111} + \psi^E_{,2222} + 2\psi^E_{,1122}\right],\end{aligned} \tag{D.6}$$

thus $\nabla \cdot \boldsymbol{u}_\gamma = \nabla^2\kappa^E$.

Now for the curl we have

$$\begin{aligned}\nabla \times \boldsymbol{u}_\gamma &= \partial_1\left(\gamma_{2,1} - \gamma_{1,2}\right) - \partial_2\left(\gamma_{1,1} + \gamma_{2,2}\right) \\ &= \gamma_{2,11} - \gamma_{2,22} - 2\gamma_{1,12}.\end{aligned} \tag{D.7}$$

The shear component derivatives are

$$\begin{aligned}\gamma_{2,11} &= \psi^E_{,1112} + \frac{1}{2}\left(\psi^B_{,1111} - \psi^B_{,1122}\right) \\ \gamma_{2,22} &= \psi^E_{,1222} + \frac{1}{2}\left(\psi^B_{,1122} - \psi^B_{,2222}\right) \\ \gamma_{1,12} &= \frac{1}{2}\left(\psi^E_{,1112} - \psi^E_{,1222}\right) - \psi^B_{,1122},\end{aligned} \tag{D.8}$$

and putting it all together we get

$$\begin{aligned}\nabla \times \boldsymbol{u}_\gamma &= \cancel{\psi^E_{,1112}} - \cancel{\psi^E_{,1222}} - \cancel{\psi^E_{,1112}} + \cancel{\psi^E_{,1222}} + \frac{1}{2}\left[\psi^B_{,1111} - \psi^B_{,1122} - \psi^B_{,1122} + \psi^B_{,2222} + 4\psi^B_{,1122}\right] \\ &= \frac{1}{2}\left[\psi^B_{,1111} + \psi^B_{,2222} + 2\psi^B_{,1122}\right].\end{aligned} \tag{D.9}$$

For $\nabla^2\kappa^B$ we have

$$\begin{aligned}\nabla^2\kappa^B &= \frac{1}{2}\nabla^2\left[\psi^B_{,11} + \psi^B_{,22}\right] \\ &= \frac{1}{2}\left[\psi^B_{,1111} + \psi^B_{,2222} + 2\psi^B_{,1122}\right],\end{aligned} \tag{D.10}$$

and thus $\nabla \times \boldsymbol{u}_\gamma = \nabla^2\kappa^B$.